Monthly Notices of the ROYAL ASTRONOMICAL SOCIETY

MNRAS **549,** 1–23 (2026)
Advance Access publication 2026 May 18

https://doi.org/10.1093/mnras/stag939

JADES Data Release 4 – Paper II. Data reduction, analysis, and emission-line fluxes of the complete spectroscopic sample

J. Scholtz [1,2★†] S. Carniani [3★†] E. Parlanti [3] F. D'Eugenio,[1,2] E. Curtis-Lake,[4] P. Jakobsen [5,6] A. J. Bunker [7] A. J. Cameron [7] S. Arribas,[8] W. M. Baker [9] S. Charlot [10] J. Chevellard,[7] C. Circosta,[11] M. Curti [12] Q. Duan,[1,2] D. J. Eisenstein [13] K. Hainline,[14] Z. Ji,[14] B. D. Johnson,[13] G. C. Jones [1,2] N. Kumari [15] R. Maiolino [1,2,16] M. V. Maseda [17] M. Perna,[8] P. G. Pérez-González,[8] T. Rawle,[18] M. Rieke [14] P. Rinaldi,[19] B. Robertson,[20] A. Saxena [7,16] I. Shivaei,[8] M. S. Silcock [4] Y. Sun [14] B. Rodríguez Del Pino,[8] S. Tacchella [1,2] H. Übler [21] G. Venturi [3] C. C. Williams,[22] C. N. A. Willmer,[14] C. Willott[23] and J. Witstok [5,6]

Affiliations are listed at the end of the paper

Accepted 2026 March 23. Received 2026 March 16; in original form 2025 October 8

ABSTRACT

We present the fourth data release of the *JWST* Advanced Deep Extragalactic Survey (JADES), providing deep spectroscopic observations in the two GOODS fields. A companion paper presents the target selection, spectroscopic redshifts and success rates, and in this paper, we discuss the data reduction and present emission-line flux measurements. The spectroscopy in this work consists of medium-depth, deep, and ultradeep NIRSpec/MSA spectra of 5190 targets, covering the spectral range 0.6-5.5 μm and observed with both the low-dispersion prism (R = 30-300) and all three medium-resolution gratings (R = 500-1500). We describe the data reduction, analysis and description of the data products included in this data release. In total, we measured 3297 robust redshifts out of 5190 targets, spanning a redshift range from $z = 0.5$ up to $z = 14.2$, including 974 at $z > 4$. This data release includes 1D and 2D fully reduced spectra with 3- and 5-pixel extractions, with slit-loss corrections and background subtraction optimized for point sources. Furthermore, we provide redshifts and SNR > 5 emission-line flux catalogues for the prism and grating spectra, as well as new guidelines to use these data products. Lastly, we are launching a new JADES online data base, designed to enable quick selection and browsing of this data release. Altogether, these data provide the largest statistical sample to date including both PRISM and medium grating spectra across full NIRSpec wavelength range to characterize the properties of galaxy populations across cosmic time.

Key words: galaxies: evolution – galaxies: high-redshift.

1 INTRODUCTION

Since the launch of *James Webb Space Telescope* (*JWST*) nearly four years ago, the observatory has revolutionized our view of the Universe and early galaxy evolution. Many of these discoveries were possible due to the amazing capabilities and sensitivity of the NIRSpec instrument (P. Jakobsen et al. 2022). These discoveries include e.g.: confirmation of $z > 10$ galaxies (E. Curtis-Lake et al. 2023; P. Arrabal Haro et al. 2023; B. Wang et al. 2023; S. Carniani et al. 2024; M. Castellano et al. 2024; Y. Harikane et al. 2024; T. Y.-Y. Hsiao et al. 2024; V. Kokorev et al. 2025; R. P. Naidu et al. 2025; J. Witstok et al. 2025), many with detected emission lines (A. J. Bunker et al. 2023; M. Castellano et al. 2024; F. D'Eugenio et al. 2024b; R. P. Naidu et al. 2025; J. Scholtz et al. 2025a), from which chemical abundances have been derived (e.g. M. Curti et al. 2023; K. Nakajima et al. 2023; Y. Isobe et al. 2025; X. Ji et al. 2025), the discovery of existance of massive, quiescent and old galaxies at z = 3-5 (e.g. A. C. Carnall et al. 2023; K. Glazebrook et al. 2024; P. G. Pérez-González et al. 2024; W. M. Baker et al. 2025a; A. de Graaff et al. 2025a; A. Weibel et al. 2025); the first 'mini-quenched' galaxies (T. J. Looser et al. 2024; V. Strait et al. 2023; W. M. Baker et al. 2025b); neutral-phase outflows in massive quiescent galaxies (S. Belli et al. 2024; F. D'Eugenio et al. 2024a; R. L. Davies et al. 2024; F. Valentino et al. 2025); the discovery of metal-poor active galactic nuclei (e.g. D. D. Kocevski et al. 2023; H. Übler et al. 2023; R. Maiolino et al. 2024b; I. Juodžbalis et al. 2025; J. Scholtz et al. 2025b; R. Maiolino et al. 2025); the most distant active galactic nuclei (AGNs; R. Maiolino et al. 2024a; A. D. Goulding et al. 2023); and even tentative evidence of the first generation of stars (E. Vanzella et al. 2023; R. Maiolino et al.

★ E-mail: js2685@cam.ac.uk (JS); stefano.carniani@sns.it (SC)
† These authors contributed to this work equally.

2024b; K. Nakajima et al. 2025; E. Vanzella et al. 2025). However, for spectroscopy, the large samples are either still relatively shallow (such as Rubies and WIDE; A. de Graaff et al. 2025b; M. V. Maseda et al. 2024), or the deep observations have small number statistics, limited to tens to hundreds of objects (T. J. Looser et al. 2023; M. Curti et al. 2024; K. Nakajima et al. 2023). The key to large-scale characterization of the galaxy population at high redshift is a large sample of deep spectroscopic observations, which are able to disentangle the complex mechanisms in galaxy evolution. Indeed, at a low redshift ($z < 1$), there has been a significant investment of resources to create samples of hundreds of thousands of spectroscopic observations of galaxies (e.g. K. N. Abazajian et al. 2009; S. P. Driver et al. 2018; DESI Collaboration 2016). Studies focusing on multiple physical properties of galaxies at once (e.g. G. Kauffmann et al. 2003a, b; Y.-j. Peng et al. 2010; G. J. Graves & S. M. Faber 2010), or deploying new machine-learning algorithms (e.g. A. F. L. Bluck et al. 2022; W. M. Baker et al. 2022; S. Barsanti et al. 2023; M. Walmsley et al. 2023; M. Koller, R. Maiolino & W. M. Baker 2025), have made enormous progress in galaxy evolution, unveiling the links between star-formation, stellar ages, supermassive black hole mass, metallicity, morphology and environment. Furthermore, within the last two decades, there has been a push for large spectroscopic ground-based surveys which have enabled the community to study several hundreds of galaxies up to $z = 4$ (e.g. M. Kriek et al. 2015; E. Wisnioski et al. 2015; J. P. Stott et al. 2016). Within the next few years, new facilities and surveys will expand this number to up to 1 million galaxies at $z \lesssim 4$ (G. Dalton et al. 2012; N. Tamura et al. 2016; R. S. de Jong et al. 2019; R. Maiolino et al. 2020). However, currently only *JWST* can obtain deep rest-frame optical and UV spectra for a large sample of galaxies above $z>4$, which is essential to study the early phases of galaxy evolution.

The major progress at $z>4$ has been enabled by the NIRSpec Micro Shutter Assembly (MSA; P. Ferruit et al. 2022a), which was designed to observe more than two hundred targets with a single pointing. This high multiplicity slit spectroscopy is combined with the unprecedented collecting area of the *JWST* mirror, low background and nominal wavelength coverage up to 5.5 μm. As a result, we are now able to observe rest-frame optical and UV emission of a large sample of galaxies $z > 4$ (e.g. T. Treu et al. 2022; R. Bezanson et al. 2024; S. Fujimoto et al. 2023; P. A. Oesch et al. 2023; A. J. Bunker et al. 2024, hereafter B24).

With these goals and capabilities in mind, the *JWST* Advanced Deep Extragalactic Survey (JADES; D. J. Eisenstein et al. 2023a), took spectra of more than 2207 galaxies at redshifts $z > 3$, enabling us to shift our focus from discovering high-redshift galaxies to statistically investigating their properties. To maximize the efficiency of this process, JADES is a combined collaboration of *JWST* NIRCam and NIRSpec GTO teams to fully exploit the combination of imaging and spectroscopic data. The JADES survey strategy is split into the three tiers: medium-depth, deep-depth and ultradeep-depth (for the shallowest and widest tier of the NIRSpec GTO see M. V. Maseda et al. 2024), targeting the two GOODS fields (Great Observatories Origins Deep Survey; M. Giavalisco et al. 2004). While the medium tiers were observed in both GOODS South and North fields (hereafter GOODS-S and GOODS-N), the two deepest tiers focused on GOODS-S only. There were three previous data releases (DRs): (i) DR 1, which is split between imaging (M. J. Rieke et al. 2023) and spectroscopy (B24); (ii) DR2, which provided new GOODS-S imaging (D. J. Eisenstein et al. 2023b); and (iii) DR3, which represented a significant proportion of the total survey imaging and spectroscopic data across GOODS-S and GOODS-N (F. D'Eugenio et al. 2025, referred to as DE25).

In this work and along with E. Curtis-Lake et al. (2026; hereafter Paper I), we present the final data release of the spectroscopic part of JADES with final medium and deep observations in GOODS-S, as well as full re-reduction and re-analysis of the previous observations presented in DE25. In this data release, we provide fully reduced and calibrated 1D and 2D spectra, NIRCam image cutouts for our spectroscopic targets, as well as measurements of redshift and emission-line fluxes across two distinct extractions.[1] The sample selection, redshifts and recovered redshift success rates of the JADES spectroscopic survey are described in Paper I. We briefly describe the observing strategy in Section 2 and our new data reduction in Section 3. We then outline the measurements of spectroscopic redshifts and line fluxes (Sections 4 and 5). In Sections 6 and 7 we present an assessment of the data products and guidelines for their use. We conclude with a short summary and brief outlook (Section 8). Throughout this work, we use the AB magnitude system (J. B. Oke & J. E. Gunn 1983).

2 NIRSPEC/MSA OBSERVATIONS

All observations used NIRSpec in Multi-Object Spectroscopy mode, with the NIRSpec/MSA (P. Ferruit et al. 2022a). The MSA configurations were planned using the prioritization schemes detailed in Paper I, and the strategy described in D. J. Eisenstein et al. (2023a). The sample selection of our GTO programme is designed to understand the star-formation history at high redshifts ($z \gtrsim 5.7$), where galaxies are predominantly selected based on their rest-frame ultraviolet properties, and the mass-assembly history at lower redshifts where objects are selected from their rest-frame optical. Rare or interesting targets are also added as 'oddballs'. Objects with lower number densities are generally given a higher priority, while more numerous galaxies occupy the lower priority classes.

Here we briefly describe the observing strategy. Each visit is planned with a set of target acquisition (TA) objects (stars and compact galaxies), which were identified in the same images as those used to find positions of the science targets, to ensure the astrometry of the target acquisition sources and the science observations is identical. The TA stars were selected based on the availability of NIRCam data at the time of planning the observations. The first NIRSpec observations by JADES in GOODS-S and GOODS-N relied on MSATA stars selected from the *HST*/WFC3 H160W 100 mas imaging from CHArGE.[2] The pre-selection of sources was done by using GAIA reference stars and selecting the brightest pixel in a 3×3 pixel box centred at the nominal location of each reference star but rejecting the candidate if any of the surrounding 41×41 pixels were brighter than 20 per cent of that brightest pixel associated with the star. Because of the paucity of stars in the GOODS-N and GOODS-S regions, the selection criteria had to be relaxed so that steep profile galaxies could be selected as well.

As soon as NIRCam imaging became available ($\sim$ 31 mas resolution) we switched to the new imaging. We considered the selection of MSATA sources with flux within a 0.1 arcsec aperture in the *F150W* filter, ranging between 30 nJy and 8000 nJy to ensure the objects had good signal-to-noise detection, but still

[1] Available on the JADES website and hlsp page.
[2] https://gbrammer.github.io/projects/charge/.

far from saturation and within the permissible range for using the MSATA (for more information, see JDOCS page[3]). Additional criteria involved the concentration of light using aperture photometry (CIRC4 < 1.5∗CIRC2 and CIRC6 < 1.67∗CIRC2) and shape (minor_axis/major_axis > 0.75, FWHM < 13 pixels), all of these measured from the detection image.

Objects that passed the brightness criterion were then examined for the presence of nearby sources (bright and faint) within a radius of 0.3 arcsec, and whether bright companions (magnitude difference ≤ 2) were found within 3.2 arcsec. If either condition was true, the source was rejected. The final list of candidates was visually inspected, and objects that had a companion within 3.2 arcsec, substructure, or diffuse appearance were removed from the sample. All TAs used the NIRSpec CLEAR filter and the longest readout time (mode NRSRAPIDD6) since the TA objects in the GOODS fields are faint. Further details on the TA setups are provided in D. J. Eisenstein et al. (2023a). All TAs performed for our observations have been successful.

As described in detail by DE25, there were several technical issues with JADES NIRSpec observations, which resulted in some visits being skipped or partially collected either due to guide-star acquisition or re-acquisition failures from the Fine Guidance Sensor and 'shorts' (electrical short circuits with the NIRSpec MSA; T. D. Rawle et al. 2022). For partially collected observations of MSA configurations, the strategy was to return to the MSA configuration one year later to ensure successful completion of our programme with the selected targets. For cases where no data were obtained for an MSA configuration, we have re-planned the observation at either the same position or at a different orientation.

In Table 1, we present the complete summary of JADES NIRSpec observations, including the typical integration time (we provide the minimum, mean and maximum integration time for each spectral configuration). As our observing strategy, we use the `nrsirs2` readout mode (improved reference sampling and subtraction, or `irs`^{2}; B. J. Rauscher et al. 2012, 2017). We generally describe the observations with a label structured as 'depth/selection', where depth is either 'Medium', 'Deep', or 'Ultradeep', and selection is either '*HST*' or '*JWST*', depending on how the majority of targets was selected; these labels are then 'translated' into the `TIER` column in the published tables, and are part of the file names for the published spectra.

The full details of what is new to this data release are provided in section 2.2 of Paper I, though we provide here an overview of the completely new sets of observations being included. In the following subsections, we provide additional details on the new observations being published in this data release; the rest of the descriptions are in DE25 and B24. The DR4 electronic files provide more details, such as observation date and actual integration times per target.

We are including in this data release two tiers that were previously unpublished:

(i) 1286: GOODS-S Medium/*JWST*: Program ID 1286 is the main GOODS-S Medium/*JWST* program. These observations were planned in the same way as those of GOODS-N Medium/*JWST*, each with three sub-pointings separated by ≈

[3]https://jwst-docs.stsci.edu/jwst-near-infrared-spectrograph/nirspec-observing-strategies/nirspec-msata-reference-star-selection-recommended-strategies#gsc.tab = 0.

Table 1. Summary of JADES NIRSpec/MSA observations. Under each disperser, we report the (minimum/mean/maximum) exposure times; the minimum exposure time can be 0 for a small number of individual objects, due to disobedient shutters (for PRISM) and for protecting high-priority targets from overlap (for the gratings).

PID	Field	Depth	Selection	Tier name	PRISM (h)	G140M (h)	G235M (h)	G395M (h)	Targets	Initial release
1210	GOODS-S	Deep	*HST*/*JWST*	`goods-s-deephst`	(9.2/16.5/27.7)	(2.3/ 4.1/ 7.0)	(2.3/ 4.1/ 7.0)	(2.3/ 4.1/ 7.0)	253	B24
1180	GOODS-S	Medium	*HST*	`goods-s-mediumhst`	(0.9/ 1.0/ 4.3)	(0.9/ 1.0/ 4.3)	(0.9/ 1.0/ 4.3)	(0.9/ 1.0/ 4.3)	677	DE25
1180	GOODS-S	Medium	*JWST*	`goods-s-mediumjwst1180`	(0.3/ 2.1/ 5.2)	(0.9/ 1.8/ 4.3)	(0.9/ 1.8/ 4.3)	(0.9/ 1.8/ 4.3)	533	DE25
1181	GOODS-N	Medium	*HST*	`goods-n-mediumhst`	(0.6/ 2.0/ 6.9)	(0.9/ 1.0/ 3.5)	(0.9/ 1.0/ 3.5)	(0.9/ 1.0/ 3.5)	853	DE25
1181	GOODS-N	Medium	*JWST*	`goods-n-mediumjwst`	(0.3/ 1.6/ 5.2)	(0.9/ 1.7/ 5.2)	(0.9/ 1.7/ 5.2)	(0.9/ 1.7/ 5.2)	950	DE25
3215	GOODS-S	Ultradeep	*JWST*	`goods-s-ultradeep`	(2.8/32.4/61.6)	(2.8/ 7.7/11.2)	–	(11.2/23.0/33.6)	228	DE25
1286	GOODS-S	Medium	*JWST*	`goods-s-mediumjwst`	(0.5/ 2.1/ 2.2)	(0.7/ 2.1/ 2.2)	(0.9/ 2.4/ 2.6)	(0.9/ 2.4/ 2.6)	1490	This work
1287	GOODS-S	Deep	*JWST*	`goods-s-deepjwst`	(9.2/16.5/27.7)	(2.3/ 4.1/ 7.0)	(2.3/ 4.1/ 7.0)	(2.3/ 4.1/ 7.0)	235	This work

1 arcsec. Compared to DE25, all observations from this programme are now included, with the new observations from October and December 2023. For this visit, the integration times per sub-pointing in some dispersers were reduced from 3.1 to 2.7 ks to fit within the available time allocation.

(ii) 1287: GOODS-S Deep/*JWST*: Program ID 1287 is the main GOODS-S Deep/*JWST* programme, which shares the observational setup with GOODS-S Deep/*HST*, but different pointings with three dither positions, each achieving 9.3 h on source exposure, as well as 2.3 h per grating per dither position. Given the design of the observations, many targets were observed up to 27 h in Prism and 7 h in the gratings.

With this release, we include a table containing the redshifts, target information used for mask preparation, and emission-line measurements. We label this table as the `Master`. We summarize the main properties of each target in the `Master` table. The columns of this table are described in Table 2. We note that the order of the targets in the `Obs_info` table is the same as subsequent tables for PRISM and R1000 flux measurements described in Section 7.1.

3 NIRSPEC/MSA DATA REDUCTION

3.1 Description of the GTO pipeline

The data processing for this release is based on the latest version of the NIRSpec GTO pipeline version 5.1, with the Calibration Reference Data System context file of jwst1413.pmap. The overall structure of the pipeline is similar to that described in B24 and DE25, although several steps have been updated and automated to minimize user intervention and ensure consistent results across the various tiers. This section provides a detailed description of the main steps included in the data processing workflow (Fig. 1).

At the core of the NIRSpec GTO pipeline is the extraction of calibrated spectra from NIRSpec count-rate images retrieved directly from the MAST archive. The count-rate maps are created using the pipeline build 12.0.5 using the context references file CRDS_CTX jwst_1303.pmap. This process relies mainly on the NIRSpec Instrument Performance Simulator pipeline software (NIPS; B. Dorner et al. 2016) developed by the ESA NIRSpec Science Operations Team. NIPS was designed with three primary objectives: (a) to process pre-*JWST* simulations (G. Giardino et al. 2019), (b) to support data processing during commissioning (e.g. N. Lützgendorf et al. 2022), and (c) to develop and validate algorithms for inclusion in the standard STScI pipeline. These algorithms are described in C. Alves de Oliveira et al. (2018) and P. Ferruit et al. (2022), and have all been incorporated into the STScI pipeline (C. Alves de Oliveira et al. 2018). Due to licensing restrictions, limited resources for user support, documentation, and code maintenance, ESA-developed Python packages are not publicly released.

Over the past three years, the NIRSpec GTO team has updated or replaced several components of the NIPS pipeline to optimize the quality of the final data products in alignment with the scientific objectives of the JADES program. In addition, the data processing workflow has been fine-tuned based on a default MSA configuration that has been used in all JADES tiers and programs. This configuration involves allocating three contiguous shutters perpendicular to the spectral dispersion direction for each target, followed by a three-point nodding pattern (0, ±1) along the

Table 2. Structure of the `Obs_info` target table for the Data Release 4.

Column name	Description
`Unique_ID`	Unique ID of the source in the survey
`PID`	*JWST* Programme ID
`TIER`	Name of subset
`TIER_old`	Old name of subset in previous DR
`NIRSpec_ID`	ID of the target in eMPT
`NIRCam_DR5_ID`	NIRCam ID from upcoming DR5
`NIRCam_DR3_ID`	NIRCam ID from DR3 (DE25)
`ObsDate`	Date of observations
`RA_TARG`	Target right ascension (deg)
`Dec_TARG`	Target declination (deg)
`x_offset`	Intra-shutter target offset (arcsec)
`y_offset`	Intra-shutter target offset (arcsec)
`Field`	Name of field (GS or GN)
`GSa`	Selection method used for GOODS-S field – a[a]
`GSb`	Selection method used for GOODS-S field – b[a]
`PC_empt`	Priority class within empt software
`Priority`	Priority class in target assignment process
`oddball_source`	Source catalogue used for oddball selection
`PC_eMPT_pre_oddball`	Priority class within empt software before it was selected as oddball
...	
`priority_pre_oddball`	Priority class in target assignment process before it was selected as oddball
...	
`probability_allocated`	Probability of being allocated an MSA shutter
`F444W_gold_DR3`	Gold sample based on `F444W` in DR3 photometry[a]
...	
`UV_gold_DR3`	Gold sample based on UV magnitude in DR3 photometry[a]
...	
`F444W_gold_DR5_beta`	Gold sample based on `F444W` in upcoming DR5 photometry[a]
...	
`UV_gold_DR5_beta`	Gold sample based on UV magnitude in upcoming DR5 photometry[a]
...	
`assigned_Prism`	`True` if has prism observations
...	...
`assigned_G395H`	`True` if has G395H observations
`nDither_Pr`	Number of dithers for prism
`nDither_Gr`	Number of dithers for gratings
`nInt_Prism`	Number of integrations for prism
...	...
`nInt_G395H`	Number of integrations for G395H
`tExp_PRISM`	Exposure time for prism (s)
...	...
`tExp_G395H`	Exposure time for F290LP/G395H (s)
`Filt_overlap`	List of affected filters by overlap
`Targ_overlap`	List of targets overlapping the spectrum for each filter
`wlmin_overlap`	min target wavelength affected by the overlap
`wlmax_overlap`	max target wavelength affected by the overlap
`wlmin_ov_overlap`	min wavelength of the target doing the overlap
`wlmax_ov_overlap`	max wavelength of the target doing the overlap
`z_Spec`	Redshift (both prism and gratings)
`z_Spec_flag`	Redshift flag (both prism and gratings)
`z_paper`	Redshift from previously published work
`z_paper_name`	Name of the object in the previous work
`z_paper_ref`	Citation to the previous work
`z_PRISM`	Prism-based redshift
`z_R1000`	Grating-based redshift
`z_R1000n`	Number of emission lines used to identify Grating-based redshift
`1500A_flux`	1500 Å flux
`1500A_flux_err`	1500 Å flux error
`MUV`	Absolute UV magnitude
`MUV_err_u`	Absolute UV magnitude upper error
`MUV_err_l`	Absolute UV magnitude upper lower

[a]For the selection method, refer to Paper I.

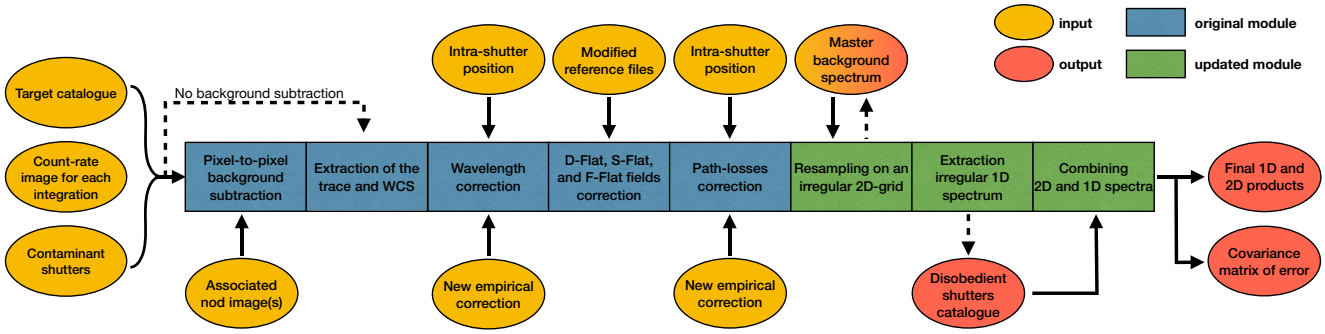

Figure 1. Outline of the overall workflow of the GTO NIRSpec/MSA pipeline. The blue and green indicate the original and updated modules in the workflow. The yellow and red regions show the input and output of the pipeline, respectively.

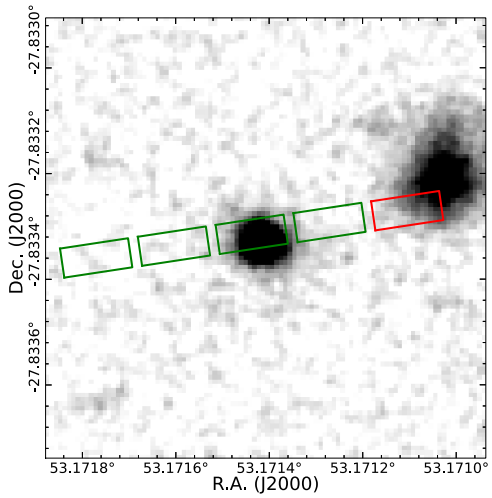

Figure 2. *F277W* NIRCam 5 arcsec × 5 arcsec cutout of the JADES target 86727 in the tier goods-s-mediumjwst. The MSA shutters corresponding to the three-point nod pattern are overlaid on the image. The green-outlined shutters are those processed by the NIRSpec GTO pipeline for background subtraction and target spectrum extraction. The red-outlined shutter is excluded from the background subtraction process due to contamination of its trace by light from a non-target galaxy.

resulting slitlet. All algorithms developed for the NIRSpec GTO pipeline are available upon request.

Fig. 1 illustrates the NIRSpec GTO pipeline workflow, highlighting both the original NIPS steps and the updated modules developed by the GTO team. The pipeline processes the 2D count-rate products delivered by the MAST archive and treats each 2D count-rate image corresponding to each integration as an independent exposure. Another key input is the observed target catalogue, which includes the position of the targets in the MSA array and their locations within the shutter pitch. Additionally, the pipeline requires a supplemental catalogue, labelled 'contaminated shutters' in Fig. 1, which lists all open MSA shutters that may contribute spectral traces to the detector due to the presence of an emitting source in those open shutters. As described below, this catalogue is crucial for background subtraction. It is generated by overlaying the open shutter positions onto available NIRCam or *HST* images and identifying overlaps with galaxies in the open shutter aperture (Fig. 2). We adopt a conservative approach by exploiting the NIRCam (or *HST* where no NIRCam imaging is present) segmentation maps to verify if each failed open shutter overlaps any source in the segmentation map.

Table 3. Nominal and JADES wavelength ranges of the disperser–filter combinations.

Disperser–filter	Nominal range	JADES range
PRISM/CLEAR	0.6-5.3	0.6-5.45
G140M/F070LP	0.70-1.27	0.70-2.20
G235M/F170LP	1.66-3.07	1.66-4.00
G395M/F290LP	2.87-5.10	2.87-5.48
G395H/F290LP	2.87-5.14	2.87-5.14

The pipeline executes eight default processing steps:

(i) *Pixel-to-pixel background subtraction*. For each target, the background emission is subtracted directly from the count-rate image using one or two shutters of the assigned slitlet that are free from contamination by other galaxies or extended emission from the target itself. This step is optional and may be skipped. As discussed in the next step, non-background-subtracted data can be used to identify problematic shutters and to create a global master background spectrum.

(ii) *Extraction of the trace and assignment of the world coordinate system*. The pipeline extracts sub-images for each target, containing the spectral trace across three shutters, and assigns wavelength and spatial coordinates to each pixel. Spectral traces are extracted beyond the nominal wavelength range specified in the NIRSpec documentation for both R100 and R1000 observations, where there is still non-negligible throughput of the instrument. The wavelength ranges for each spectral configuration are summarized in Table 3 and shown in Fig. 3.

(iii) *Wavelength correction*. A wavelength zero-point correction is applied to account for the intra-shutter position of each target. The correction map is provided in the WAVECORR reference file, which is based on Fourier optical simulations carried out prior to the *JWST* launch (P. Jakobsen et al. 2022). However, even after applying this correction, a wavelength offset discrepancy remains between emission lines measured in spectra obtained with the R1000 and R100 modes in previous data releases (e.g. DE25) and in other surveys (e.g. A. de Graaff et al. 2025b). We investigated this wavelength offset in detail and identified a correlation with both the wavelength and the intra-shutter position of the target along the dispersion direction. Based on this, we derived an additional, data-driven correction map that reduces the discrepancy between data obtained with the grating and the prism. This ad-

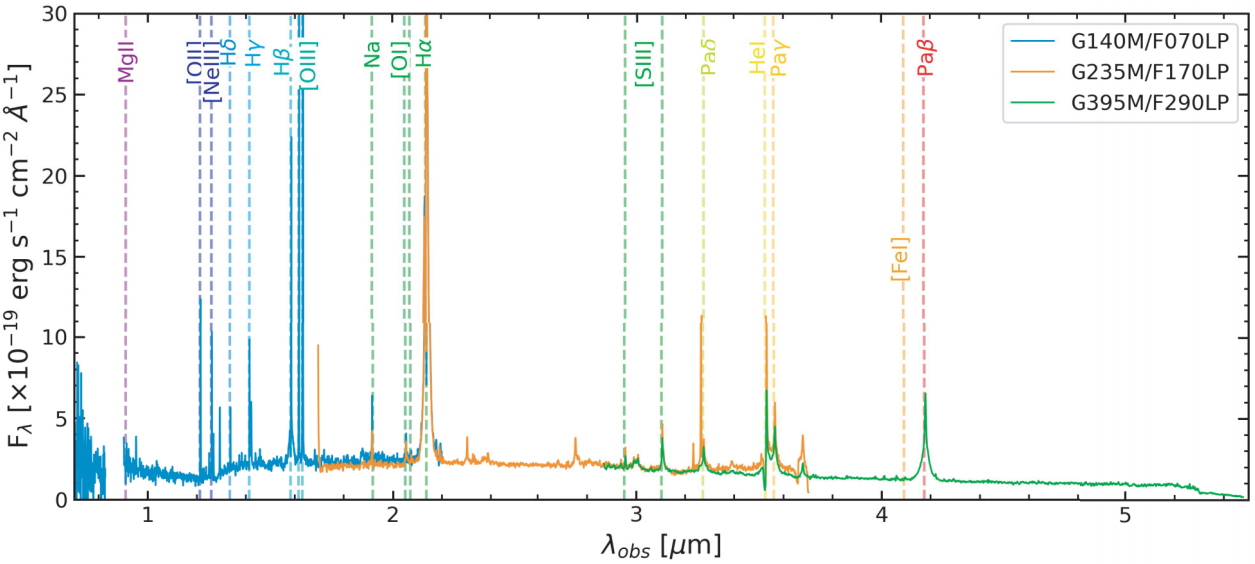

Figure 3. Illustration for the expanded wavelength coverage of gratings and the agreement in the flux calibration between the gratings of < 10 per cent, even in the extended wavelength range. This object, `NIRSpec_ID` 28074 from `goods-n-mediumhst` has been dubbed the Rosetta Stone of the Little Red Dots (I. Juodžbalis et al. 2024).

ditional correction has been applied to the current data release. Further details of this analysis are provided in Section 6.1.

(iv) *Flat-field correction*. The unrectified trace of each target is corrected using the detector response curves called D-flat, S-flat, and F-flat curves (T. D. Rawle et al. 2016). The D-flat characterizes how each pixel responds to different wavelengths, incorporating both quantum efficiency and the spectral performance of the anti-reflection coating. The F-flat accounts for throughput losses caused by reflections within the telescope and instrument optics, as well as the transmission properties of the selected filter. The S-flat describes how variations in aperture size and position affect the optical path of the light as it passes through different instrument components. For this data release, the Calibration Reference Data System (CRDS) context jwst1413.pmap was used. However, as mentioned above, we have extended the calibration beyond the nominal wavelength ranges of R1000 configurations to fully exploit the wavelength coverage of the spectrograph (see Table 3). Appendix A discusses how the transmission curve of each individual flat-field reference file was extrapolated beyond the nominal wavelength range.

(v) *Path-loss correction*. A correction is applied for path losses, accounting for the deviation from a perfectly centred point source. This wavelength-dependent correction assumes a point-like source geometry for all targets and uses the intra-shutter position of the target to determine the correction. Because the MAST archive includes observations of individual stars (PID 1133), we estimated the pathloss correction map directly from the data. This map provides correction factors as functions of both source position within the aperture and wavelength (see details in Appendix B).

(vi) *Resampling onto a rectified 2D grid*. This is one of the first modules modified by the NIRSpec GTO team members. In this step the extracted spectral traces are rectified onto a two-dimensional grid using an algorithm by B. Dorner (2012), which is similar to 'drizzle' (A. S. Fruchter & R. N. Hook 2002). The only distinction between the two algorithms is in the method used to estimate the variance. In the standard drizzle algorithm, the equation used to compute the variance includes the 'fractional pixel overlap' squared (equation 7 in A. S. Fruchter & R. N. Hook 2002). Although this is mathematically correct, A. S. Fruchter & R. N. Hook (2002) noted that this approach underestimates noise on larger spatial scales because it neglects the covariance terms introduced when data from a single input pixel are distributed over multiple output pixels. To compensate for this effect, the variance equation includes the fractional pixel overlap in linear form rather than squared. This results in an increase of approximately 15 per cent in the uncertainty for each individual output pixel but preserves the total noise level when integrating over multiple output pixels (B. Dorner 2012). In the context of our final 1D spectra, the uncertainty is accurate only when estimated over a number of spectral channels corresponding to the line spread function and not at the level of individual spectral channels. A more precise noise estimate would require computation of the full covariance matrix. However, this is only feasible for those targets observed in more than 20 exposures, as detailed in K. N. Hainline et al. (2024), S. Carniani et al. (2024) and J. Witstok et al. (2025).

(vii) *Extraction of master background spectrum*. If the background subtraction step is skipped, the user can opt to have the pipeline generate a master background 2D image. This is done by computing the median of the 2D rectified, calibrated traces from all three-shutter slitlets designated as 'sky'. The resulting master background image can then be subtracted from the 2D spectrum of the target to remove background emission. Based on our experience in the JADES program, background removal using the master background image is generally less accurate than the standard pixel-to-pixel subtraction method, particularly for compact galaxies. However, the master background approach can be advantageous for bright, extended galaxies, where diffuse emission contaminates all shutters of the slitlet assigned to the target. This step has been included in the NIRSpec GTO pipeline workflow, but is not yet implemented in this data release.

(viii) *Extraction of 1D spectrum*. In this step, the pipeline extracts 1D spectra from the rectified 2D maps. The 1D extraction is performed using boxcar apertures centred on the expected intra-shutter positions of the sources, as determined from their coordinates in the MSA input catalogue. We find that the catalogue positions along the cross-dispersion direction are consistent with the photometric centroid of the 2D spectrum, within an uncertainty of 0.04 arcsec, corresponding to approximately 0.4 detector pixels (see Appendix C for details). By default, a 5-pixel-wide aperture is used, corresponding to the width of a single open shutter. Additional extraction widths of 3 pixels is also available. A 3-pixel-wide aperture is optimal for compact sources and to optimize the signal-to-noise ratio (SNR) of the final products.
The extraction process accounts for the data quality array, similar to the procedure adopted in the STScI pipeline. Specifically, pixels flagged as `DO NOT USE`, `SATURATED`, `OUTLIER`, `PERSISTENCE`, `DEAD`, `HOT`, and `OTHER BAD PIXEL` are excluded from the extraction.
If the background subtraction step is skipped, the individual PRISM/CLEAR 1D spectra are analysed to identify unexpected closed shutters. The pipeline measures flux levels in the non-background-subtracted 1D spectra and flagged as 'disobedient' those shutters which failed to open resulting in 1D spectra with a zero emission level.

(ix) *Combination of 2D and 1D Spectra*. In this final step, the pipeline combines all available 2D and 1D spectra for each target, excluding exposures affected by disobedient shutters. The data are combined using inverse-variance weighting and the data quality array. For 2D spectra, alignment is performed based on the intra-shutter positions listed in the input catalogue.
Prior to combination, the pipeline masks pixels with significantly negative flux values as these are considered unphysical and typically arise from outliers or serendipitous self-subtracted emission in the slitlets. A sigma-clipping algorithm is then applied to remove remaining outliers. This algorithm flags as outliers any pixels that deviate by more than three standard deviations from the mean value at each wavelength channel. However, this algorithm generally requires a minimum of six exposures per target to perform an appropriate outlier rejection. The pipeline, therefore, provides two versions of the final combined spectra: one with and one without sigma clipping, allowing users to assess data quality.
It is important to stress that the final 1D spectrum is not extracted from the combined 2D map. Instead, it results from the combination of individual 1D spectra. This approach is more rigorous as it avoids inaccuracies that may arise from varying intra-shutter positions across different visits, which can alter the cross-dispersion surface brightness profile due to path-loss effects. If more than 20 exposures are available for a given target, the covariance matrix of the combined spectrum is computed from 2000 bootstrap realizations, following the methodology described in K. N. Hainline et al. (2024) and J. Witstok et al. (2025). The full details of this algorithm and a comprehensive analysis of correlated noise in the final spectra will be presented in Jakobsen et al. (in preparation).
To optimize the SNR of the spectra based on the galaxy morphology, the pipeline also extracts 1D spectra from the combined 2D maps using the optimal extraction technique described by K. Horne (1986). Specifically, we constructed a normalized spatial profile along the cross-dispersion direction at each wavelength, masking the negative features associated with nod subtraction used for pixel-by-pixel background removal. If the peak of the normalized spatial profile is less than five times its associated uncertainty, the algorithm combines adjacent wavelength channels to improve the accuracy of the profile. In cases where the signal remains below this threshold across the entire wavelength range, a 5-pixel boxcar aperture centred on the catalogue-based expected target position is adopted for the 1D extraction.

For this data release, we applied the NIRSpec GTO pipeline three times by default for PRISM/CLEAR observations. First, we processed the data without background subtraction in order to identify disobedient shutters. Next, the pipeline was run with standard background subtraction, extracting 1D spectra using both 3- and 5-pixel apertures. Finally, we reprocessed the data considering only exposures from the top and bottom shutters of the three-shutter slitlets, excluding those where the target was positioned in the central shutter. This additional processing step helps mitigating self-subtraction effects in extended galaxies during background removal. In the case of observations using two nod positions, we also performed spectral extractions with both 3- and 5-pixel aperture widths in the cross-dispersion direction. For the R1000 and R2700 observations, the pipeline was applied following the same approach used for the PRISM/CLEAR data, with the exception of the initial run without background subtraction. Instead, the list of disobedient shutters identified from the R100 data was adopted for processing the higher-resolution observations, but only when these were obtained shortly after the PRISM observations and without any MSA reconfiguration.

3.2 GTO pipeline versus *JWST* Science Calibration Pipeline

Most of the steps and algorithms of the NIRSpec GTO pipeline are similar to those encapsulated within the official *JWST* Science Calibration Pipeline. However, there are some differences in the workflow that might improve the quality of the final products:

(i) *Identification of contaminants in the 3-shutter slitlet*. This step improves pixel-by-pixel background subtraction by identifying and removing off-scene nods that are contaminated by galaxies near the targets that fall in one of the free-target shutter. Without this correction, light from these galaxies would be included in the predicted background emission and subtracted from the spectrum of the target, artificially reducing its observed emission. For this step, we adopt a conservative approach that automatically verifies whether any non-target source identified in the NIRCam (or *HST*) segmentation map (B. E. Robertson et al. 2026) falls within any of the shutters dedicated to background estimation in each nod.

(ii) *New wavelength correction based on the position of the target in the shutter.* The current version of the *JWST* Science Calibration Pipeline performs a wavelength zero-point correction for an off-centre target, but the model used by this step is not sufficient to calibrate the wavelength array, which causes a spectral offset between grating and prism data. Indeed, MAST final products reveal a systematic spectral offset between the line centroids measured from the prism spectra and those measured in the grating data (Fig. D1). This spectral offset is dependent on the location of the target in the MSA shutter, the NIRSpec GTO pipeline adopts a new data-based model to perform the wavelength calibration which corrects the systematic spectral offset between grating and prism.

(iii) *Identification of disobedient shutters.* This step identifies shutters that are unexpectedly closed. Such disobedient shutters produce noisy 1D and 2D spectra lacking both background and

No.	Name	Type	Columns
0	PRIMARY	PrimaryHDU	
1	EXTRACT5PIX1D	BinTableHDU	
2	EXTRACT3PIX1D	BinTableHDU	
3	EXTRACTOPT1D	BinTableHDU	
4	INTERMEDIATE	BinTableHDU	
5	REGION	BinTableHDU	
6	F090W	Image	
7	F150W	Image	
8	F277W	Image	
9	F444W	Image	

target emission. If not excluded during the combination process, they can corrupt the final spectra. The NIRSpec GTO pipeline automatically detects these failed shutters and removes them from the data processing workflow.

3.3 High-level science products

The full suite of reduced data products for the JADES programs is available at MAST as a High Level Science Products (HLSP) via https://archive.stsci.edu/hlsp/jades, https://mast.stsci.edu/hlsp, and https://jades-survey.github.io. This release provides reduced 1D and 2D spectra with multiple options for data processing and 1D spectral extraction. Specifically, the data are processed in two ways: (1) using all three nods for each target (default workflow), and (2) using only the exposures from the top and bottom microshutters ('2 nods') for both the pixel-by-pixel background subtraction and the combination process. In the context of the extraction of 1D spectra, we use the default full shutter aperture ('5 pix') and the small box-car aperture of 3 pixels ('3 pix') centred at the target's location. We also include the 1D spectrum obtained from the combined 2D spectrum by using the optimal extraction algorithm ('opt').

The 1D and 2D spectra are available for each spectral configuration and field reported in Table 1 according to the following convention:

- *hlsp_jades_jwst_nirspec_<TIER> −<NIRSpec_ID>_<filter> − <grating>_v2.0 − spec1d.fits*
- *hlsp_jades_jwst_nirspec_<TIER> − <NIRSpec_ID>_<filter> − <grating>_v2.0 − spec2d.fits*

Here, < *TIER*> and < *NIRSpec_ID*> are the name of the tier and the ID of the NIRSpec target, respectively. < *filter*> and < *grating*> refer to the disperser–filter combination used in the observations. The fits files of the 1D PRISM/CLEAR spectra have this structure:

Here, EXTRACT5PIX1D, EXTRACT3PIX1D, and EXTRACTOPT1D products provide the '5 pix', '3 pix', and optimal 1D spectra extracted from the 2D maps, respectively. Each table includes both the spectra obtained with the standard '3-nod' scheme and those derived using only the '2-nod' exposures. For the default nodding scheme, we also report the '5 pix' 1D spectra extracted from all individual exposures in the INTERMEDIATE extension. The fits file also includes four wide-band flux-calibrated NIRCam images of 5 arcsec×5 arcsec around the target (see B. D. Johnson et al., 2026, for details of the NIRCam reduction). Finally, the extension REGION is a FITS Region binary table reporting the corner positions of the slitlets used for the target in pixel units, which can be used directly in the attached NIRCam images, and the respective RA and Dec in the International Celestial Reference System (ICRS).[4] We note that this extension is supported by DS9. The 1D HLSP related to the observations obtained with the grating have the same structure but they do not include the NIRCam cutout images.

No.	Name	Type
0	PRIMARY	Image
1	FLUX	Image
2	FLUX_ERR	Image
3	WAVELENGTH	Image
4	FLUX_2NOD	Image
5	FLUX_ERR_2NOD	Image
6	OPT_PROFILE	Image
7	OPT_PROFILE_2NOD	Image

The 2D HLSP fits files have this structure:

Here, FLUX and FLUX_ERR illustrate the combined flux-calibrated 2D maps from the standard '3 nod' scheme, while the 2D maps for the '2 nod' data processing workflow are included in the extension FLUX_2NOD and FLUX_ERR_2NOD. The wavelength array is reported in WAVELENGTH. Finally, the OPT_PROFILE and OPT_PROFILE_2NOD extensions provide the 2D 'weighting' profiles estimated by the optimal extraction algorithm and used to extract the spectra from the combined 2D maps.

4 PRISM EMISSION-LINE FLUXES

The method used to fit the PRISM spectra is the same as outlined in DE25. In order to fit the PRISM spectra with the underlying strong continuum, we use the spectral fitting software PPXF (M. Cappellari 2023), which models the data as a linear combination of physically motivated spectral templates to ensure that the underlying stellar absorption (in particular Balmer absorption) is accounted for in the emission-line fluxes. As input templates, we considered a set of simple stellar population templates from FSPS (SSP; C. Conroy, J. E. Gunn & M. White 2009). The templates were calculated using MIST isochrones (J. Choi et al. 2016), the C3K model atmospheres (C. Conroy et al. 2019), and a Salpeter initial mass function (E. E. Salpeter 1955). The templates have higher resolution ($R = 10\,000$) between $0.1 < \lambda < 3$ μm, compared to the PRISM resolution of $R = 50$–300. The templates are available from C. Conroy upon reasonable request. To reduce degeneracies, we only consider a subset of templates, which spans ages in the range of 0.03-20 Gyr and metallicities [Z/H] −2.5-0 in logspace. For each target, we also adjust the grids to ensure that the oldest available SSP is consistent with the age of the Universe at the redshift of the fitted target, save a buffer of one age bin (see e.g. T. J. Looser et al. 2023). The initial value for the redshift for the fitting was determined based on the visual inspection described in DE25.

In addition to the stellar templates, we also fit a set of Gaussian models to represent the nebular emission lines in the data. These nebular/gas templates can be divided into three separate cate-

[4]We note that the astrometric solution for GOODS-N changed between target selection and final NIRCam reductions (see Johnson et al., 2026). We include an average, per-object shift to the shutter regions but caution that there is an additional level of uncertainty in their exact positions due to these changes.

Table 4. List of the emission lines fit in the prism spectra. All wavelengths are in a vacuum.

	Line(s)	λ [Å]	z range	Column name	Notes
	C IVλλ1549,1551	1549.48	—	C4_1549	
	He IIλ1640 +O III]λλ1661,1666	1650.00	—	Blnd_He2_O3_1650	
	C III]λλ1907,1909	1907.71	—	C3_1907	
	Mg IIλλ2796,2803	2799.94	—	Mg2_2796	
	[O II]λλ3726,3729	3728.49	—	O2_3727	
	[Ne III]λλ3869,3968	3869.86,3968.59	$0 < z < 5.3$	Ne3_3869,Ne3_3968	
	[Ne III]λ3869	3869.86	$z \geq 5.3$	Ne3_3869	
	[Ne III]λ3968 +Hε	3968.59	$z \geq 5.3$	Ne3_3968	
	Hδ	4102.86	—	HD_4102	
	Hγ +[O III]λ4363	4341.65	$0 < z < 5.3$	Blnd_HG_O3	
{	Hγ	4341.65	$z \geq 5.3$	HG_4341	
{	[O III]λ4363	4363.44	$z \geq 5.3$	O3_4363	
{	Hβ	4862.64	$0 < z < 2$	Blnd_HB_O35007d	
{	[O III]λλ4959,5007	4960.30,5008.24	$0 < z < 2$		
{	Hβ	4862.64	$2 \leq z < 5.3$	HB_4861	
{	[O III]λλ4959,5007	4960.30,5008.24	$2 \leq z < 5.3$	O3_5007d	
{	Hβ	4862.64	$z \geq 5.3$	HB_4861	
{	[O III]λλ4959,5007	4960.30,5008.24	$z \geq 5.3$	O3_4959,O3_5007	
	He Iλ5875	5877.25	—	He1_5875	
	[O I]λλ6300,6363	6302.05,6363.67	—	O1_6300	
{	Hα +[N II]λλ6548,6583	6564.52	$0 < z < 2$	Blnd_HA_N2_S2	
{	[S II]λλ6716,6731	6725.00	$0 < z < 2$		
{	Hα +[N II]λλ6548,6583	6564.52	$z \geq 2$	HA_6563	
{	[S II]λλ6716,6731	6725.00	$z \geq 2$	S2_6725	
	He Iλ7065	7067.14	—	He1_7065	
	[S III]λλ9069,9532	9071.10,9533.20	—	S3_9069,S3_9532	
	Paδ	10052.12	—	PaD_10049	
{	He Iλ10829	10832.06	—	He1_10829	
{	Paγ	10940.98	—	PaG_10938	
	Paβ	12821.43	—	PaB_12818	
	Paα	18755.80	—	PaA_18751	

Note. The set of templates used to fit any given galaxy depends on its initial redshift guess; this is because the spectral resolution of the prism is a strong function of wavelength (P. Jakobsen et al. 2022), causing emission-line groups to be spectrally resolved or unresolved at different redshifts. Empty redshift ranges indicate the template is used at all redshifts. Rows connected by curly braces indicate emission-line pairs/groups that have tied velocity and velocity dispersion.

gories: (i) single Gaussian components representing individual emission lines (or doublets/multiplets that are completely unresolved) that are spectrally isolated at any redshift at the resolution of the PRISM observations (e.g. He I λ5787, Paβ); (ii) single Gaussian component representing the spectrally blended lines given the resolution of PRISM (e.g. Hα + [N II] λλ6548, 6583, Hγ + [O III] λ4363); and (iii) two Gaussian components representing doublets with fixed ratios (e.g. [O III] λλ4959, 5007, [S III] λλ9069, 9532). We summarize the emission-line templates and their redshift range in Table 4. We note that the exact set of templates that we use in the fitting is dependent on the sources' initial redshift, since the spectral resolution of the prism is strongly evolving with wavelength, making some emission-line groups spectrally resolved or unresolved at different redshifts. Following A. J. Cameron et al. (2024) and DE25, we also include a step function that is designed to capture the strong Balmer jumps that appear in some of our objects.

We set bounds on the linear combination coefficients to be always positive. Finally, we also use a 10th-order multiplicative Legendre polynomial to adapt the shape of the continuum to the data; this can be thought of as a combination of physical effects (e.g. dust reddening) and flux calibration issues (e.g. incorrect slit-loss corrections, for extended objects and for objects with strongly wavelength-dependent morphology, flat fielding effects, etc.). Before we start the PPXF run, each template is convolved to match the spectral resolution of the data; we use the nominal resolution, boosted by a factor of 1/0.7. The reason for the increased effective resolution is that the nominal resolution is given for the case of a uniformly illuminated shutter, while in the case of distant galaxies (especially those at very high redshifts) they are typically smaller than the shutter width, hence their size sets the effective resolution (A. de Graaff et al. 2023). A similar resolution boost has been adopted independently by other works (e.g. J. E. Greene et al. 2024). We remark that we do not use the derived line widths from the prism. We truncate the templates to match the rest-frame wavelength range of our data. The stellar templates are set to zero blueward of Lyα, i.e. we do not include this region in the fit. Finally, we convolved the templates with an instrumental line spread function, which is modelled as a Gaussian shape.

Overall, we run our PPXF fitting twice for each galaxy. During the first fit, we fixed the templates' kinematics subsets, constraining them to have the same central velocity and velocity dispersion. The kinematic groups are: Balmer lines and stellar templates, rest-frame UV lines, rest-frame optical lines and rest-frame NIR lines. After the initial round of fitting, we discard any emission lines that are not detected at least 5σ significance.

During the second run, we fix the kinematics of the stellar continuum absorption, use only previously detected emission-line templates, and remove almost all kinematic groups. Exceptions to the latter rule are: the blend group formed by [S II] λλ6716,

Table 5. List of the emission lines fit in the medium-resolution grating spectra. All wavelengths are in a vacuum. Rows connected by curly braces indicate emission lines that were fitted using the same redshift and FWHM during the same fit because they are sufficiently close in wavelength that the continuum can be modelled simultaneously.

Line(s)	λ [Å]	Column name
C IV$\lambda\lambda$1549,1551	1549.48	C4_1549
He IIλ1640	1640.00	He2_1640
O III]$\lambda\lambda$1661,1666	1663.00	O3_1663
C III]$\lambda\lambda$1907,1909	1907.71	C3_1907
[O II]$\lambda\lambda$3726,3729	3728.49	O2_3727
[Ne III]λ3869	3869.86	Ne3_3869
Hδ	4102.86	HD_4102
Hγ	4341.65	HG_4341
[O III]λ4363	4363.44	O3_4363
Hβ	4862.64	HB_4861
[O III]$\lambda\lambda$4959,5007	4960.30,5008.24	O3_5007
He Iλ5875	5877.25	He1_5875
[O I]$\lambda\lambda$6300,6363	6302.05	O1_6300
Hα	6564.52	HA_6563
[N II]$\lambda\lambda$6548,6583	6585.27, 6549.86	N2_6584
[S II]$\lambda\lambda$6716,6731	6718.29, 6732.67	S2_6718, S2_6732
He Iλ7065	7067.14	He1_7065
[S III]$\lambda\lambda$9069,9532	9071.10,9533.20	S3_9069,S3_9532
Paδ	10052.12	PaD_10049
He Iλ10829	10832.06	He1_10829
Paγ	10940.98	PaG_10938
Paβ	12821.43	PaB_12818
Paα	18755.80	PaA_18751

6731 and the blend Hα + [N II] $\lambda\lambda$6548, 6583; the group formed by Hβ and [O III] $\lambda\lambda$4959, 5007; the group formed by Hγ and [O III] λ4363; and the group of He I λ10830 and Pa γ, whose kinematics are always tied together. It is important to note that He I λ10830 is resonant; therefore, this emission line tends to be redshifted relative to the systemic velocity of the target; however, leaving the line kinematics free relative to Paγ tended to produce bad fits due to low spectral resolution. Therefore, we opted to keep these lines tied. This setup closely follows the one outlined in DE25, as it is necessary due to the limited spectral resolution of the prism observations.

After each fit, we post-process the line fluxes as follows. Below redshift $z < 2$, we combine Hβ and [O III] $\lambda\lambda$4959, 5007 and Hα + [N II] $\lambda\lambda$6548, 6583 and [S II] $\lambda\lambda$6716, 6731; the line uncertainties are added in quadrature. Between $2 \leq z < 5.3$, we combine the flux from the [O III] $\lambda\lambda$4959, 5007 doublet. The best-fitting spectra are carefully inspected for any artefacts or failed fits, either due to low equivalent width emission lines near the Balmer break, emission lines due to contaminants, outliers, etc. The low equivalent width emission lines near the Balmer break arise when the shape of the break is not fit correctly, and the algorithm may use [O II] $\lambda\lambda$3726, 3729, [O III] $\lambda\lambda$4959, 5007, [Ne III] $\lambda\lambda$3869, 3968, and H δ to add to the continuum. Contaminants and artefacts may escape the sigma-clipping in PPXF when they fall close to strong emission lines in the intended target.

5 MEDIUM-RESOLUTION-GRATING EMISSION-LINE FLUXES

We fitted the medium-resolution spectra using `QubeSpec`'s[5] fitting module, specifically designed for NIRSpec/MSA observations. We fitted each emission line with a single Gaussian component and the continuum with a simple power law. Although this is a simplistic approach, it is perfectly adequate for describing a narrow range of the continuum around an emission line of interest ($\pm$100 Å), as usually the continuum is poorly detected. The majority of the emission lines are fitted in isolation, except for a group of emission lines that are close to each other, such as Halpha, [N II] and [S II]. We show the full list of emission lines fitted in this work and the groups fitted together in Table 5 along with names of the emission lines in our public release.

To estimate the model parameters, we use a Bayesian approach implemented with the Markov chain Monte Carlo (MCMC) integrator `emcee` (D. Foreman-Mackey et al. 2013). To measure the emission-line fluxes, redshifts and widths, we need to set prior probabilities for each of the variables. The peaks of the Gaussian profiles and the continuum normalization are given a log-uniform prior, while the FWHMs are set to a uniform distribution spanning from the minimum spectral resolution of the NIRSpec/M-grating ($\sim$200 km s^{-1}) and 800 km s^{-1}. The prior on the redshift was a truncated normal distribution centred on the redshift from the visual inspection and with a standard deviation of 300 km s^{-1} and with a maximum allowed deviation of 1000 km s^{-1}. As described in the PRISM flux fitting in Section 4, the redshift prior was centred on the value from the visual inspection of both PRISM and R1000 data described in DE25.

We fit only a single Gaussian per emission line in the medium-resolution grating. We note that there are some objects with detected outflows or broad line regions. The potential type-1 AGNs have been investigated in (I. Juodžbalis et al. 2025) and broad components in forbidden lines associated with outflows will be presented in S. Carniani et al. (in preparation).

After the initial fitting run, we visually inspect every model for any incorrect fits or spurious line detection that are caused by unflagged outliers or other problems. These flagged fits are then

[5] https://github.com/honzascholtz/Qubespec.

Table 6. Structure of the grating flux table. The initial rows are the same as for the prism (between `NIRSpec_ID` and `z_PRISM`; cf. Table 7); all fluxes are in units of $\times 10^{-18}$ erg s^{-1} cm^{-2}.

Column name	Description
`Unique_ID`	Unique ID of the source in the survey
`PID`	Program ID
`TIER`	Name of subset[a]
`TIER_old`	Old name of subset used in DR1 and DR3
`NIRSpec_ID`	ID of the target in eMPT[a]
`NIRCam_DR5_ID`	NIRCam ID from upcoming DR5
`NIRCam_DR3_ID`	NIRCam ID from DR3 (DE25)
`z_R1000`	R1000-based redshift
`z_R1000n`	Number of emission lines used to determine the best R1000 redshift
`[name]_flux`	Emission-line flux
`[name]_err`	Emission-line flux uncertainty
`[name]_SNR`	SNR emission line based on 50th/16th percentile of the posterior distribution
`[name]_filter`	Emission-line disperser/filter

[a]`NIRSpec_IDs` are not unique in the table, but the combination of `NIRSpec_ID` and `TIER` is unique.

refitted and re-inspected to ensure sufficient quality. The final fluxes are calculated using the MCMC chains (after discarding the burn-in chains – 50 per cent) and the final reported values and their uncertainties are the median value and standard deviation from the chains. We estimated the SNR of an emission line as the 50 per cent/16 per cent of the posterior distribution of the emission-line flux. This ensures we correctly estimate the SNR of an emission line for lines with highly asymmetric posterior distribution of emission-line flux. The final redshift from the medium-resolution spectra is the redshift inferred as a weighted average of emission lines with an SNR >5.

The structure of the grating emission-line catalogue is presented in Table 6 where the fluxes are in units of $\times 10^{-20}$ erg s^{-1} cm^{-2}. The names of the individual emission-line columns are the same as reported in Table 5. For the emission-line doublets with fixed line ratios (such as [N II] λλ6548, 6583 and [O III] λλ4959, 5007) we only report the flux of the stronger emission line. Alongside the fluxes and their uncertainties, the initial rows are the same as for the prism table.

Given the spectral overlap of the gratings, some emission lines are measured in two adjacent gratings. For emission lines that lie in the spectral range where the gratings overlap, we fit both sets of data. We do not attempt to stack these spectral overlaps due to different line spread functions and potential flux calibration offsets between the gratings that can bring further uncertainties into the fit. The final emission-line measurements are primarily chosen from the redder of the available disperser, unless the emission line is not covered by the instrument due to the detector. We include a column in the final R1000 table (`eml_name_filter`) indicating the grating/filter combination used to estimate the value in the table. Furthermore, we also add `ext` to the name of the disperser/filter combination to indicate when the emission line was extracted outside of the nominal spectral range of NIRSpec disperser/gratings presented in Table 3.

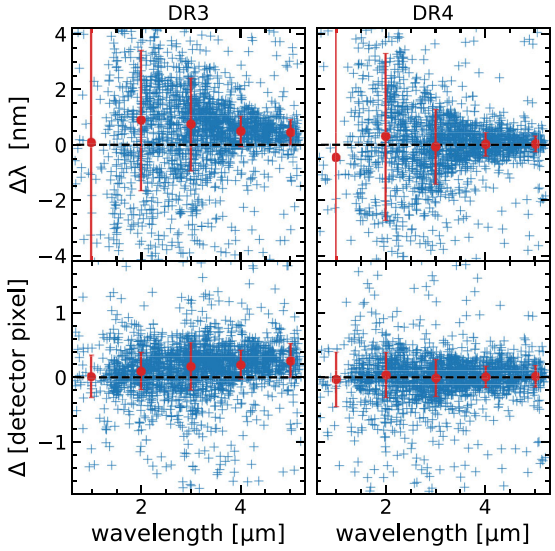

Figure 4. Comparison of the line centroids of [O III], H α, and He I measured in the prism and grating data for DR3 (left) and DR4 (right). The top panels show the wavelength offset in units of nm, while the bottom panels report the spectral offset in units of detector native prism pixels. Red marks show the median and standard deviation values of the distribution of measurements at 1, 2, 3, 4, and 5 μm.

6 QUALITY ASSESSMENT

In this section, we perform the quality assessment of the data reduction and the data analysis. In Section 6.1 we describe the accuracy of the wavelength calibration, in Sections 6.2 and 6.3 we describe the absolute flux calibration of our data products along with the comparison of the prism and gratings observations, and in Section 6.4 we describe the quality of our redshift estimates.

6.1 Accuracy of the wavelength calibration

Several *JWST* studies have reported a discrepancy between redshifts measured from prism and grating data for the same targets (e.g. A. J. Bunker et al. 2023; F. D'Eugenio et al. 2025; A. de Graaff et al. 2025b). To investigate the origin of this discrepancy and to identify a possible empirical solution, we exploited the extensive JADES data set. Initially, we processed the data using the same pipeline employed for DR3, but updated with the latest standard reference files from the Calibration Reference Data System (CRDS; see Section 2). We then measured the spectral centroids of emission lines in both the prism and grating data, focusing on the brightest lines: [O III], H α, and He I across all redshifts. In the right panels of Fig. 4 we show the offset between the two observational modes, expressed both in wavelength and in native detector pixel units. We found a systematic offset ranging from 0.5 to 2.1 nm, corresponding to approximately 0.15–0.3 detector pixels for the prism. The variation of the offset in wavelength units is strongly wavelength-dependent, primarily due to the non-uniform spectral resolution of the prism across its wavelength range. For this reason, all further analysis was carried out in detector pixel units to minimize the impact of this dependence.

Our analysis revealed that the spectral offset correlates with the intra-shutter position of the target along the dispersion direction. A similar result was also reported by DE25 and A. de Graaff et al. (2025b). This suggests that the centroid of the spectral point spread function, which depends on the location of the source

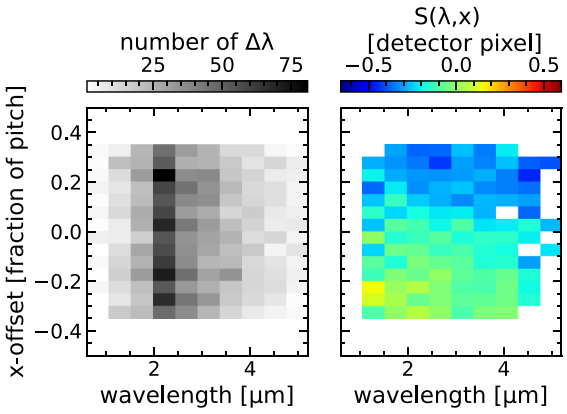

Figure 5. Empirical wavelength zero-point additional offset for a point-source as a function of wavelength and source displacement from the micro-shutter centre in the dispersion direction. The left panel shows the distribution of measurements, while the right panel reports the offset to apply to the map in addition to the predictions from the CRDS reference file.

within the shutter, is not fully accounted for in the current calibration. In particular, we suspect that the 'wavecorr' step, which is intended to update the wavelength solution based on the offset of the source from the shutter centre, does not apply a sufficiently accurate correction.

We therefore calculated the additional wavelength shifts ($S(\lambda, x)$) to apply in addition to the shift predicted by the CRDS reference file $S^{\rm ref}(\lambda, x)$. In detail, the correction can be expressed as

$$\lambda^{\rm corr} = \lambda + [S(\lambda, x) + S^{\rm ref}(\lambda, x)]\delta\lambda(\lambda) \quad (1)$$

where λ is the wavelength assigned to the detector pixel for a point source at the centre of a specific shutter of the MSA array and $\delta\lambda(\lambda)$ is the size in wavelength unit of the detector pixel. Therefore, $S(\lambda, x)$ can be estimated assuming that the centroids of the emission lines of the prism and grating are identical after applying the additional correction:

$$\begin{aligned} 0 &= \lambda^{\rm corr}_{\rm prism} - \lambda^{\rm corr}_{\rm grat} \\ &= \lambda_{\rm prism} - \lambda_{\rm grat} + [S(\lambda, x) + S^{\rm ref}(\lambda, x)][(\delta\lambda_{\rm prism}(\lambda) - \delta\lambda_{\rm grat}(\lambda)] \end{aligned}$$

Since $\delta\lambda_{\rm prism}(\lambda)$ and $\delta\lambda_{\rm grat}(\lambda)$ are known and the measured wavelength offset reported in Fig. 4 corresponds to:

$$\Delta\lambda(\lambda, x) = \lambda_{\rm prism} - \lambda_{\rm grat} + S^{\rm ref}(\lambda, x)[\delta\lambda_{\rm prism}(\lambda) - \delta\lambda_{\rm grat}(\lambda)]$$

We can map the additional $S(\lambda, x)$ correction at varying λ and intra-shutter position x as:

$$S(\lambda, x) = -\frac{\Delta\lambda(\lambda, x)}{\delta\lambda_{\rm prism}(\lambda) - \delta\lambda_{\rm grat}(\lambda)}$$

The outcome of this analysis is illustrated in Fig. 5 which reports the distribution of the number of spectral offset measurements $\Delta\lambda$ and a discrete map of $S(\lambda, x)$. The grid of the map was selected to maximize the coverage of the shutter aperture and have at least 10 measurements for each bin.

The empirical correction map $S(\lambda, x)$ was incorporated into the data-processing workflow by applying linear interpolation onto the finer grid adopted by the pipeline, and linear extrapolation at wavelengths or intra-shutter offsets not covered by our data. The interpolated map was then applied to process the spectra used in this analysis. As shown in the right panels of Fig. 4, the systematic

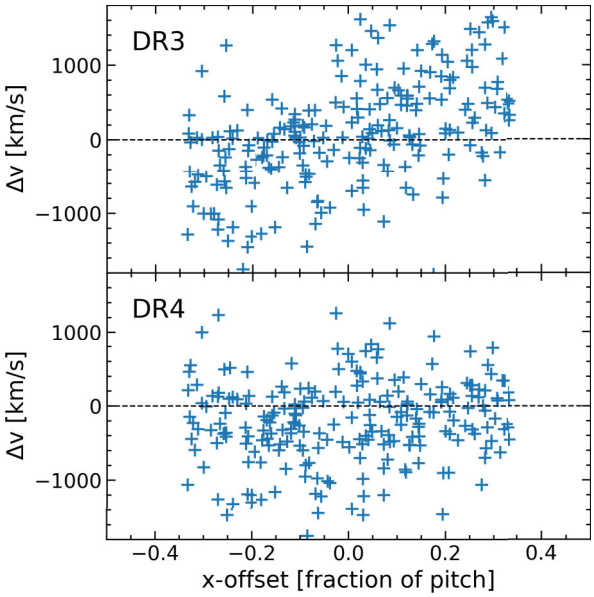

Figure 6. Wavelength calibration bias as a function of intrashutter source position for prism. Δv indicates the wavelength calibration bias as defined in equation (2), x-offset is the spatial offset of the target with respect to the centre of the shutter, measured along the dispersion direction. For an unbiased wavelength solution, we would expect $\Delta v = 0$ at any x-offset values. The top panel illustrates the same results found by DE25, indicating that the standard correction adopted for the intrashutter source position in DR3 is insufficient. The bottom panel shows the wavelength calibration bias calculated in the spectra of DR4, where we used a new data-based wavelength correction as defined in equation (1).

offset between line centroids measured in the prism and those measured in the grating is significantly reduced. However, we note a substantial scatter in the distribution of measurements, particularly at shorter wavelengths. This scatter may be attributed to both the uncertainty in centroid measurements in the prism spectra, especially at 1 μm, where the spectral resolution is low, and residual inaccuracies in the wavelength calibration associated with the spatial extension of the targets and uncertainties on the target location within the shutter.

DE25 also reported a wavelength-dependent discrepancy in redshift estimates within individual prism spectra: redshifts derived from emission lines at short wavelengths (< 2 μm) were found to differ from those based on redward lines (> 3 μm). Notably, this redshift discrepancy appears to correlate with the intra-shutter position of the target along the dispersion direction. To further investigate this effect, we performed a similar quality assessment using a sample of galaxies in the redshift range $1 < z < 3$, selected to have simultaneous detections of both [O III] and He I lines in the prism spectrum, each with an SNR exceeding 10σ. Redshifts were estimated from the He I line, and the spectral offsets were defined as

$$\Delta v = c\left(\frac{\lambda_{\rm [O\,III]}}{\lambda^{\rm rest}_{\rm [O\,III]}(z_{\rm HeI}+1)} - 1\right), \quad (2)$$

where c is the light speed, $z_{\rm HeI}$ is the redshift calculated from the helium line, and $\lambda_{\rm [O\,III]}$ and $\lambda^{\rm rest}_{\rm [O\,III]}$ are the measured and rest-frame line centroid of the oxygen line, respectively. Fig. 6 shows the spectral offset, in units of velocity, as a function of the intra-shutter position, both before and after applying our empirical

correction. Prior to the correction, we observed the same trend reported by DE25. The new correction effectively removes the systematic dependence on intra-shutter location, significantly reducing the spectral offset between redshift measurements obtained at shorter wavelengths and those estimated at longer wavelengths. However, an offset of approximately 1000 km s^{-1}, which is below the prism spectral resolution, remains visible in some individual galaxies.

6.2 Accuracy of the absolute flux calibration

In this data release, we include all computed path-loss corrections by the pipeline in the final 1D and 2D spectra (see Section 7). Using the intra-shutter position of the target and assuming a point-like source, the pipeline estimates two components of the pathloss correction: the 'geometrical' loss, which accounts for light that does not pass through the aperture, and the 'diffraction' loss, which arises from light diffracted by the aperture that is subsequently lost at the pupil plane of the instrument.

As these corrections are based on the assumption that the target is not spatially extended, we performed a quality assessment by comparing the NIRSpec PRISM fluxes with those measured from NIRCam images at the same wavelength. We therefore used the latest version of the JADES NIRCam catalogue[6] (JADES Collaboration, 2026) and cross-matched the catalogues of the targets using the coordinates associated with the 1D spectra with a searching radius of 0.1 arcsec. We then computed synthetic NIRCam photometry for all spectra at six different wavelengths using the nominal throughputs of *F090W*, *F150W*, *F200W*, *F277W*, *F356W*, and *F444W* filters, and compared it with the CIRC2 NIRCam photometries. The latter were estimated from a circular aperture of radius 0.15 arcsec, which is comparable to the open area of the NIRSpec shutters.

Fig. 7 shows the ratio of the synthetic NIRCam photometry of NIRSpec spectra and CIRC2 NIRCam photometry as a function of redshift for the six selected filters. We note that the flux level of the NIRspec spectra is consistent with the uncertainties of the NIRCam photometry. However, the intrinsic scatter of the distribution is about 0.11 dex at all wavelengths. This corresponds to a 25 per cent absolute flux accuracy of the NIRspec spectra.

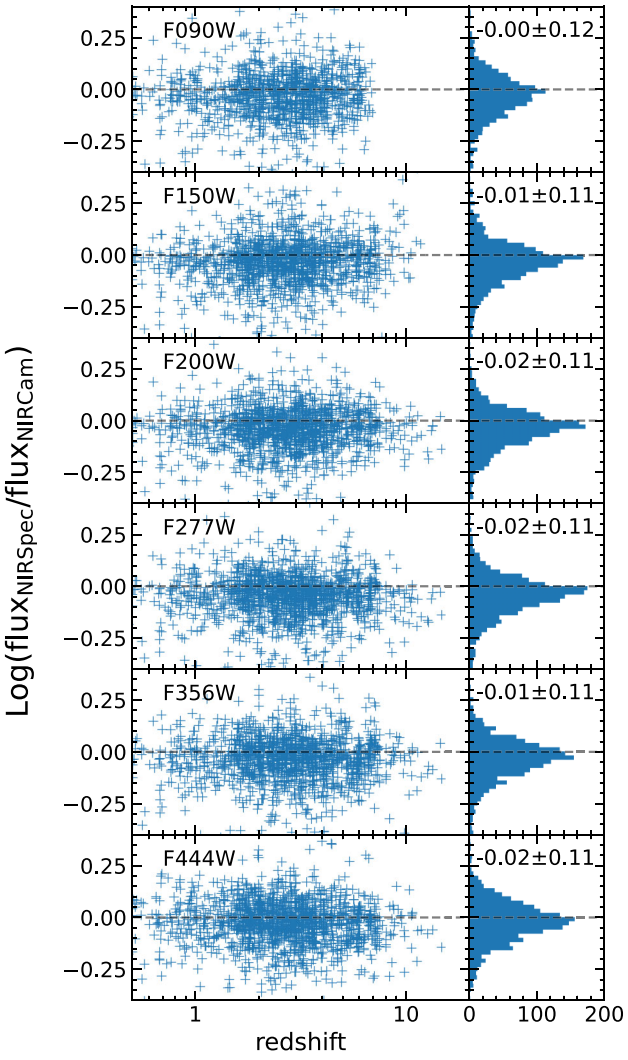

Figure 7. Left: ratio between the synthetic NIRCam photometry of NIRSpec spectra and CIRC2 NIRCam photometries from JADES NIRCam catalogue as a function of redshift for six different filters as reported in the plots. CIRC2 NIRCam photometries are extracted from a circular aperture of radius 0.15 arcsec. Right: distribution of the ratio on a logarithmic scale. The text reports the median and standard deviation of each distribution of values.

6.3 Flux calibration between PRISM and gratings

In this section, we perform a detailed comparison of the flux calibration between the PRISM and medium gratings, as well as our comparison to the DR3. As the continuum is rarely detected in the grating spectra, we compare the measured emission-line fluxes between the PRISM and grating observations, rather than to the NIRCam photometry as done above. For the emission-line flux comparison, we chose [O II] λλ3726, 3729, [O III] λλ4959, 5007, Hα + [N II] λλ6548, 6583, Hβ, [S III]λ9062, and [S III]λ9532 emission lines, as they are well isolated and bright for accurate comparison of the data releases and dispersers. We highlight the wavelength range of each of the three grating filters as shaded regions in Fig. 8.

We note that in PRISM observations, there is an increased discrepancy in [O II] λλ3726, 3729 between grating and PRISM due to the low resolution of the PRISM observations, and the effect that prominent continuum features near the Balmer limit can display a break (stellar Balmer break, e.g. T. J. Looser et al. 2024; or nebular Balmer jump, e.g. A. J. Cameron et al. 2024). When the resolution is insufficient, the strength of the break is degenerate with the flux of the nearest lines, with [O II] λλ3726, 3729 being the most affected line. This is aggravated by using an incorrect value of the spectral resolution due to the object being smaller than the slit, which increases the resolution of the observations. All these issues can significantly affect the recovered [O II] λλ3726, 3729 flux, particularly in the low-resolution regimes found at lower wavelengths (e.g. A. de Graaff et al. 2025b).

Overall, we find a mean ratio of the PRISM and grating fluxes of 1.080 ± 0.004 with a standard deviation of 0.36, consistent with the findings of B24 and DE25. The flux ratio is constant across the wavelength range of the instrument with a value above 1.5 μm of ∼1.09, showing that the individual gratings have a consistent flux calibration. Indeed, we see that the spectral regions where

[6] https://archive.stsci.edu/hlsp/jades.

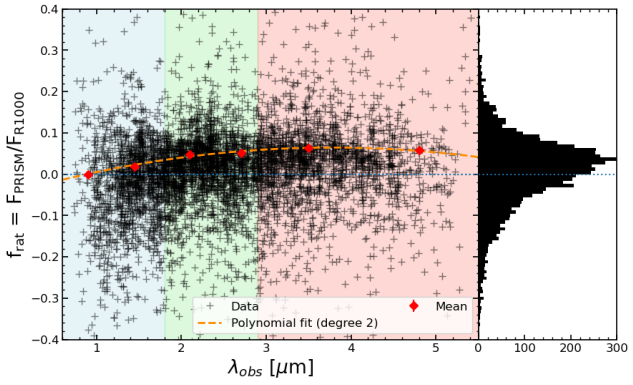

Figure 8. Ratio of the fluxes of emission lines measured from the gratings and PRISM as a function of the wavelength. We compare isolated emission lines: [O II] $\lambda\lambda$3726, 3729, [O III] $\lambda\lambda$4959, 5007, Hα + [N II] $\lambda\lambda$6548, 6583, Hβ, [S III], and [S III]. The black points show the individual measurements, while the red points show the mean in distinct bins. The orange dashed line shows the best fit to the flux offset between PRISM and R1000 described in equation (3). The blue, green, and red shaded regions indicate the three gratings G140m, G235m, and G395m, respectively. We find a mean offset between the PRISM and the grating of 8 per cent.

the grating spectra overlap the flux value and emission line are consistent.

We quantify the ratio between the PRISM and R1000 fluxes by fitting a third-order polynomial in log space as a function of wavelength. We derived the following relation:

$$\log_{10}\left(\frac{F_{\rm PRISM}}{F_{\rm R1000}}\right) = (-0.045 \pm 0.11) + (0.582 \pm 0.007) \times\lambda - (0.007 \pm 0.001)\lambda^2 \quad (3)$$

where λ is wavelength in microns. Using this function above will allow users to remove any statistical flux offsets between PRISM and R1000 fluxes.

Given the excellent consistency of the PRISM with the NIRCam imaging, we consider the PRISM observations to be correct, with the grating observations being higher by ∼10 per cent. Although this difference is not enough to influence the majority of science cases, we note that combining PRISM and R1000 observations for science cases sensitive to line ratios (such as Balmer decrement and hence attenuation curves) needs to take into account the systematic uncertainties between the dispersers.

Given that we have re-reduced the entire spectroscopic survey with new context files (see Section 3), we need to investigate any changes between the previous data release (DR3) and the one presented in this work. In Fig. 9 we compare the prism (left panel) and grating (right panel) fluxes released as part of DR3 and DR4 for the same emission lines as for Fig. 8. We show the ratios between the new and the old calibration files as a red dashed line. We see that the difference in the data releases is purely driven by the change of the calibration files rather than any other changes. We note that there are a few objects with emission-line ratios between DR3 and DR4 over a factor of 1.5 (75 emission lines in total). We note that the final ratio between the fluxes between DR3 and DR4 is a combination of both `Sflats` and `Fflats`, as well as new changes to pathloss corrections. Therefore, the new fluxes are not a simple multiplicative factor of the new calibration files but also depend on the source's location in the shutter, creating the wide scatter in the comparison and some large outliers.

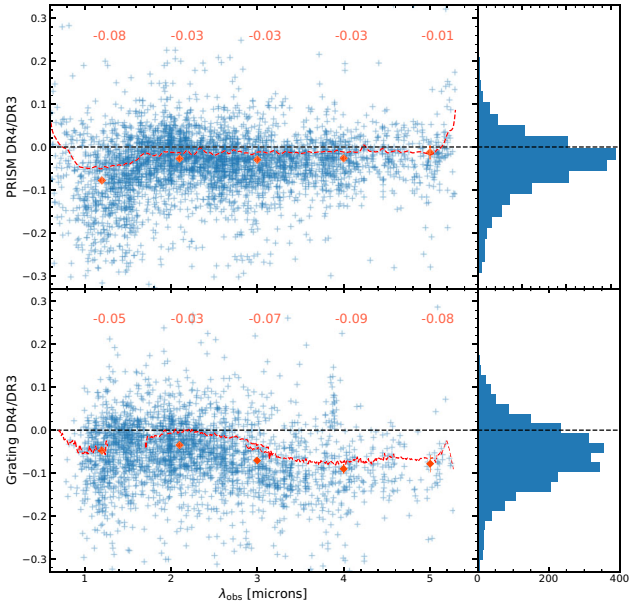

Figure 9. Ratio of the fluxes from the DR4 and DR3 for PRISM fluxes (top panel) and gratings (bottom panel). The blue points show the individual measurements. The red points show average ratios, which we also show as red numbers above the points. The dashed red line shows the ratio of the SFlats and FFlats used in the data release, while the red points show the mean in distinct bins. The changes between DR4 and DR3 can be explained by the combination of new calibration files and new pathloss corrections.

6.4 Redshift combination and comparison: prism versus medium gratings

For the final redshift estimate for an object, we combined the redshift measurements from both PRISM and gratings to allow the most accurate version of the redshift. Whenever we have a strong emission-line detection (i.e. 5 σ) in the gratings, we adopt the redshift of this emission line and give it a redshift flag A. Using a single emission line is warranted because the grating fits are done only for galaxies with a visually inspected redshift (see DE25). We have manually verified that none of our objects have discrepant redshifts between PRISM and gratings by more than $\Delta z = 0.05$, which would indicate misidentified emission lines. Furthermore, we note that any large offsets ($|\Delta z - \langle \Delta z \rangle| > 0.015$ (see end of this section) were visually inspected, and are mostly due to uncertainties in the Hβ-[O III] $\lambda\lambda$4959, 5007 blend and to low signal-to-noise data.

We assigned the redshift quality Flag B to any target for which we only have a PRISM detection of at least two independently fitted emission lines. For a combination of a strong continuum break and an emission line (i.e. less secure or precise redshifts), we assigned redshift flag C. An even lower class is reserved for redshifts identified as tentative in the visual inspection; in this case, we report the visual-inspection redshift (flag D). All other redshifts are assigned −1 (flag E). We summarize the redshift flags as follows:

(i) `[A]` Redshift from at least one emission line in the medium-resolution grating.

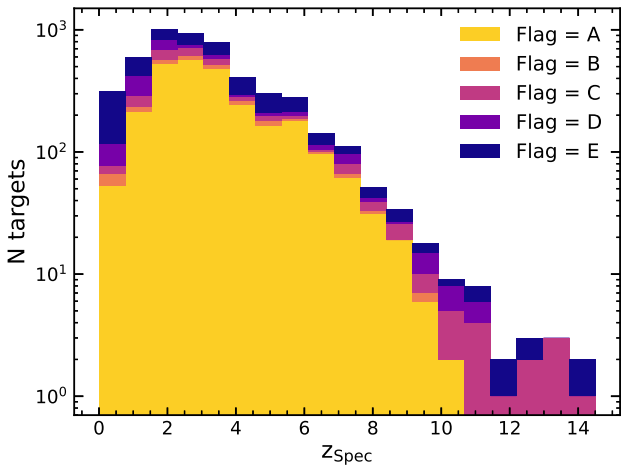

Figure 10. Redshift distribution of the sample, colour-coded by the final redshift flag (Section 6.4). We note a drop in redshift distribution at $z_{Spec} \sim 9.75$; this reflects a similar drop in the distribution of photometric redshifts of the targets selected for observation. For flag 'E' we use the photometric redshift for illustration.

(ii) `[B]` Redshift from two or more prism emission lines.
(iii) `[C]` Redshift from the continuum, or from the continuum and a single prism emission line.
(iv) `[D]` Tentative, from visual inspection.
(v) `[E]` No redshift.

Note that the first three flags are the same as in B24 and DE25. These measured redshifts and associated quality flags are also presented and used in Paper I to assess the success of our target selection strategy. We note that a full assessment of the redshift quality assessment and success of our strategy are presented in Paper I. The combined redshift distribution of the sample is shown in Fig. 10, colour-coded by flag. There is an accelerated decline in secure spectroscopic $z_{Spec} \sim 9.75$, consistent with the similar feature in the photometric redshift distribution of our source catalogue as mentioned by DE25, further exaggerated by the redshifting of [O III] λλ4959, 5007 out of the NIRSpec wavelength range, making the spectroscopic redshift reliant on fainter emission line or the Lyα break.

To view the true evolution in the UV luminosity density from the spectroscopic sample, one must take account of the survey selection function. The fraction of the underlying population sampled, as well as the redshift completeness and outlier fraction, are required for this level of calculation and are provided on a tier-by-tier basis in Paper I.

In Fig. 11 we show M_{UV} versus redshift, for the sample where magnitudes could be measured directly from the NIRSpec data; to this end, we used a nominal top-hat filter between rest-frame 1400 and 1600 Å, following the procedure outlined in A. Saxena et al. (2024). We colour-coded our points with the equivalent width of [O III] λ 5007, measured directly on the prism data (empty symbols are galaxies with no detected [O III] λ5007). We do not see any evidence for a trend between the EW of the [O III] and the M_{UV} at fixed redshift.

In Fig. 12 we compare the redshift measurements from the PRISM and from the medium gratings, for emission lines with SNR >10. In order to assess the quality of our redshifts we defined $\Delta v/c \equiv (z_{prism} - z_{gratings})/(1 + z_{prism})$, and we find a mean offset of 72 ± 8 km/s, significantly less than the values derived by B24 and

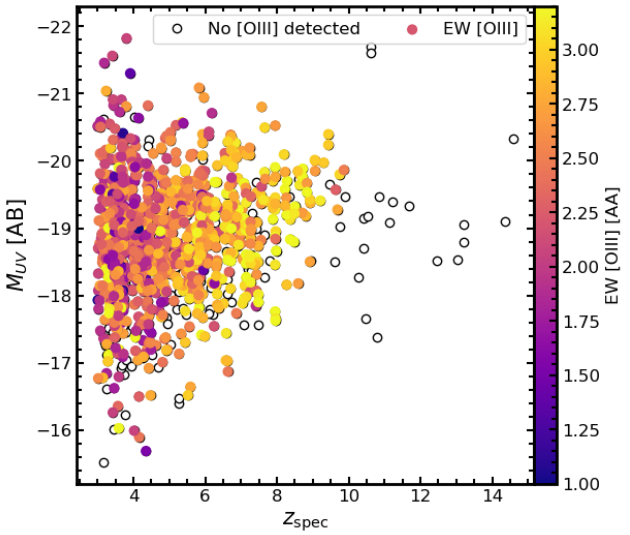

Figure 11. Redshift versus UV magnitude distribution of the sample, colour-coded by the equivalent width of [O III] λ5007 (empty symbols are galaxies with no detected [O III] λ5007). Magnitudes were calculated directly from the prism spectra, using aperture corrections estimated by comparing the prism magnitude to the 0.35-arcsec radius magnitude (`CIRC5` in the catalogues) in the NIRCam filter nearest to rest-frame 1500 Å. [O III] λ5007 falls outside of the NIRSpec wavelength range at $z \gtrsim 10.0$. For more information on the EW of [O III] λλ4959, 5007, see K. Boyett et al. (2024).

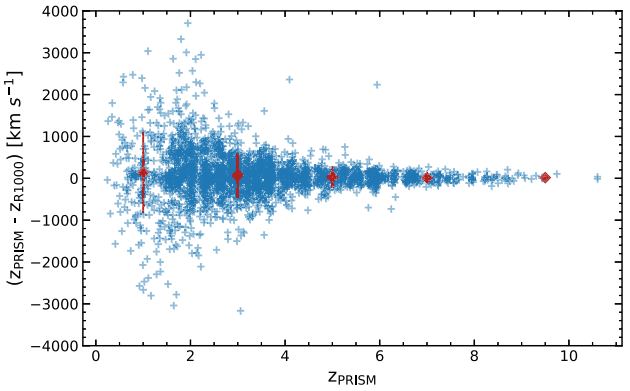

Figure 12. Comparison of redshifts between the prism and the medium-resolution gratings. We find a redshift-independent offset 72±8 km s^{-1}. The red diamonds are the moving mean, with the error bars showing the 1σ scatter in velocity offset between PRISM and R1000. The increased dispersion at low redshifts is expected from the strong dependence of the prism spectral resolution with wavelength.

DE25. We note that the scatter of this offset has a strong dependency on wavelength, or more importantly, on the native pixel size of the NIRSpec instrument, as we show with the errorbars in Fig. 12. We would like to stress that this major improvement in the velocity offsets of lines from PRISM and medium gratings is due to the additional calibrations and corrections presented in this work.

Table 7. Structure of the prism flux table. The full list of emission lines is reported in Table 4 (all fluxes are in units of $\times 10^{-20}$ erg s^{-1} cm^{-2}).

Column name	Description
Unique_ID	Unique ID of the source in the survey
PID	Program ID
TIER	Name of subset[a]
TIER_old	Old name of subset used in DR1 and DR3
NIRSpec_ID†	ID of the target in eMPT[a]
NIRCam_DR5_ID	NIRCam ID from upcoming DR5
NIRCam_DR3_ID	NIRCam ID from DR3 (DE25)
z_PRISM	Prism-based redshift
[name]_flux	Emission-line flux
[name]_flux_err	Emission-line flux uncertainty

Notes.†NIRCam_IDs are unique, but whether they match the NIRSpec_IDs depends on target selection (*HST* versus *JWST* selection), as well as on whether the NIRCam catalogue was revised after the NIRSpec observation (which may result in sources being lost to blending and to crossing the non-detection threshold).
[a]NIRSpec_IDs are not unique in the table, but the combination of NIRSpec_ID and TIER is unique.

7 USING THE NIRSPEC DATA PRODUCTS

7.1 Data products and tables

In this section, we provide details of the data products made public in this data release, their use and their limitations. The spectra are published in the same format as described in Section 3.3 on JADES and HLSP websites.[7] The catalogues prepared for this data release are published on the JADES website and through the JADES online data base (see Section 7.2).[8] The objects are in the same order in the tables/hdu extensions and are organized as follows:

(i) **Obs_info** : The master catalogue contains the basic properties for each of the targets in our observations. We summarize each of the columns in Table 2.

(ii) PRISM flux tables (3- and 5-pixel extractions): This is the table of measured fluxes in 3- and 5-pixel extractions of the PRISM spectra measured using methods described in Section 7. The structure of the columns is described in Table 7.

(iii) R1000 flux tables (3- and 5-pixel extractions): Table of the measured fluxes from the medium gratings. We describe the method of measuring the fluxes in Section 5 and we describe the table structure in Table 6.

7.2 JADES online data base

In order to make our JADES NIRSpec data release more accessible and allow fast filtering and visualization of the data, we built an online graphical interface. Within the interface, the user can search by sky coordinates (with a user-defined search radius), redshift range, redshift quality flags (described in Section 6.4), absolute UV magnitude and emission-line fluxes (Hα, Hβ and [O II] $\lambda\lambda$3726, 3729, [O III] $\lambda\lambda$4959, 5007). The user can then search and display the target selection along with available NIRCam images, R1000 fits of Hα and Hβ, PRISM spectrum, link to the FITS_map – NIRCam image visualization and link to the HLSP portal to download the available data. This online table with the displayed columns can be downloaded as a .csv file, or the user can download the entire JADES multi-hdu fits table using the Download table button. Using this graphical interface, the users can search, filter and download the sample they are interested in.

7.3 Limitations of the data release

In this section, we provide a list of limitations of the current data release. We note that our data reduction and analysis are optimized for compact sources which are common at a high redshift, the primary goal of JADES. The users of our data release are encouraged to consider these points carefully:

(i) Gold samples: The JADES survey's selection process contains many different selection criteria and classes, resulting in an overall inhomogeneous sample; however, within the individual tiers and classes, the selection was designed based on UV apparent magnitude or NIRCam *F444W* filter flux. However, the original allocated classes were determined from the best photometry available at the time, and the underlying catalogues have since evolved (see Paper I). For this reason we defined two 'gold' samples based on spectroscopic redshifts (classes A, B, and C), applying consistent rest-UV and *F444W* selections using the most up-to-date photometry covering distinct redshift ranges: $z > 5.7$ for the UV-selected sample and $1.5 < z < 5.7$ for the *F444W*-selected sample (for full description, see Paper I). With these gold samples it is possible to reconstruct the UV luminosity function and other completeness studies. We note that we deliver the UV and *F444W* gold samples based on DR3 NIRCam photometry (DE25) and upcoming DR5 NIRCam photometry (Johnson and JADES Collaboration, 2026).

(ii) Aperture correction: Our aperture corrections are optimized for compact sources and assume that the targets have a point source morphology, i.e. the spectra and the colours are inaccurate for extended sources. When estimating emission-line ratios over a large wavelength range (such as Hα/Hβ, [O III] λ5007/[O II] $\lambda\lambda$3726, 3729, Paα/Hα), we recommend using aperture corrections derived from the photometry, using the relevant NIRCam images included in the published data files for this purpose. Targets that are extended over more than one shutter should be considered with particular care, or even excluded (see background subtraction).

(iii) 3- and 5-pixel extraction: We extract the 1D spectra from the 2D spectra using two separate extractions – 3 and 5 pixels. We note that for compact, barely resolved sources, the 3-pixel extraction is more optimized for unresolved and close to unresolved sources, and the user might get better SNR compared to the 5-pixel extraction. We encourage the users to compare the measured fluxes in 3- and 5-pixel extractions to verify that they account for the total flux of the emission line in the target.

(iv) Background subtraction: Similarly to the aperture corrections, our background subtraction is optimized for compact sources; while shutters affected by contaminants are pre-identified and not considered in the subtraction, shutters affected by the same source cause self-subtraction. For these sources, the users are encouraged to use the 2-nod extraction spectra (see description of data products).

[7] https://jades.herts.ac.uk/DR4, https://jades-survey.github.io/scientists/data.html, and https://archive.stsci.edu/hlsp/jades.
[8] https://jades.herts.ac.uk/search/.

(v) Noise spectrum: Our uncertainties on the flux values are based on variance-conserving resampling, to minimize the effects of correlated noise (B. Dorner 2012) and hence are considered conservative (e.g. J. Witstok et al. 2025). A full analysis of correlated noise in NIRSpec will be presented in a future work (P. Jakobsen, in preparation).

(vi) Wavelength calibration: The updated wavelength calibration reduces the spectral offset between prism and grating data reported in DR3, leading to improved alignment in DR4. The calibration uncertainties are on the order of one-tenth of the spectral resolution of the disperser used in the observations. Larger uncertainties occur for spatially extended galaxies or when the intra-shutter position of the source is poorly constrained.

(vii) Spectral overlap: The PRISM observations were set up so that we avoid any spectral overlaps. However, for grating observations, there can be some overlap in the spectra for low-priority class observations. The users should take care to ensure these are not misinterpreted. We included additional information in the `Obs_info` regarding the overlapping spectra: (1) affected filter observations; (2) target ID overlapping the spectrum; (3) wavelength range affected; and (4) wavelength range of the object affecting the main target. With the information, the user can investigate further any potential contamination.

(viii) Flux calibration: We determine that the absolute calibration of the PRISM observations is accurate within ∼25 per cent. The relative flux calibration between the prism and gratings is accurate to within 10 per cent, and depends on the wavelength (e.g. Figs 7, 8, and 9). The user is encouraged to consider this problem when measuring flux ratios. We particularly note that estimating Balmer ratios across different gratings or between PRISM and gratings can lead to inaccurate estimates of dust extinction. We encourage users to consider the offset between PRISM and grating fluxes described by equation (3). In addition, the wavelength-dependent flux discrepancy between PRISM and gratings suggests that emission-line fluxes within the same disperser may also suffer from flux calibration issues.

8 CONCLUSIONS

In this work, we present the final JADES NIRSpec Data release which includes data obtained up to January 2025 in the two GOODS fields. The spectra include medium-depth, deep-depth, and ultra deep-depth observations (∼2–70 h on source) up to redshift $z \sim 14$, reaching the deepest unlensed spectroscopic observations to date, with up to 70 h on source. The sample size of 5190 galaxies and the data quality of spectra are a testament to the success of the MSA mode of the *JWST*/NIRSpec telescope and instrument.

This paper accompanies the release of the final calibrated spectra and the accompanying NIRCam image cutouts for each target, along with catalogues containing spectroscopic redshifts, emission-line fluxes, and observational information. The large sample has enabled us to investigate remaining calibration challenges of the NIRSpec instrument within the data reduction: (i) mismatch in the wavelength calibration between PRISM and gratings; (ii) flux calibration between the used dispersers; and (iii) background subtraction and slit-loss corrections appropriate for unresolved and extended sources. To make advancements in this section of the calibration, future calibration programmes are necessary to remove these last remaining challenges from the data. The spectra, photometry and survey completeness have been used to recover the UV luminosity function in the companion Paper I.

Future programmes aiming to significantly increase the sample size of the general galaxy population at similar redshift and stellar mass range to JADES will require a significant investment of *JWST* time, or potentially a novel observing strategy with higher observing efficiency. However, regular GO programmes should be able to observe large samples of specific rare types of objects, such as (e.g. high-redshift quiescent galaxies, extremely reddened galaxies, little red dots, $z > 8$ Lyα emitters), where the JADES survey has only scratched the surface. As we are not able to release the GTO pipeline publicly, we plan to process all public GO data and release it to the community through the JADES data base.

In the meantime, the JADES survey represents the largest sample of galaxies at a high redshift covering the full 0.6–5.5 μm with both PRISM and medium-resolution grating spectroscopy. Combining this spectroscopic data with deep medium and wide-band imaging enables the broader astronomical community to study galaxy evolution from the Cosmic Dawn to the Cosmic Noon.

ACKNOWLEDGEMENTS

This work is based on observations made with the NASA/ESA/CSA *James Webb Space Telescope*. The data were obtained from the Mikulski Archive for Space Telescopes at the Space Telescope Science Institute, which is operated by the Association of Universities for Research in Astronomy, Inc., under NASA contract NAS5-03127 for *JWST*. These observations are associated with programmes 1180, 1181, 1210, 1286, 1287, and 3215. JS, RM, FDE, and GCJ acknowledge support by the Science and Technology Facilities Council (STFC), ERC Advanced Grant 695671 'QUENCH' and the UKRI Frontier Research grant RISEandFALL. RM also acknowledges funding from a research professorship from the Royal Society. SC and EP acknowledge support from the European Union (ERC, WINGS,101040227). ECL acknowledges support of an STFC Webb Fellowship (ST/W001438/1). The Cosmic Dawn Center (DAWN) is funded by the Danish National Research Foundation under grant DNRF140. AJB, AS, and AJC acknowledge funding from the 'FirstGalaxies' Advanced Grant from the European Research Council (ERC) under the European Union's Horizon 2020 research and innovation programme (grant agreement No. 789056). WMB gratefully acknowledges support from DARK via the DARK fellowship. This work was supported by a research grant (VIL54489) from VILLUM FONDEN. DJE was supported as a Simons Investigator and by *JWST*/NIRCam contract to the University of Arizona, NAS5-02115. Support for program #3215 was provided by NASA through a grant from the Space Telescope Science Institute, which is operated by the Association of Universities for Research in Astronomy, Inc., under NASA contract NAS 5-03127. ZJ, MR, BDJ, and CNAW were supported by the *JWST*/NIRCam contract to the University of Arizona, NAS5-02115. MP acknowledges support through the grants PID2021-127718NB-I00 and RYC2023-044853-I, funded by the Spanish Ministry of Science and Innovation/State Agency of Research MCIN/AEI/10.13039/501100011033 and El Fondo Social Europeo Plus FSE+. PGP-G acknowledges support from grant PID2022-139567NB-I00 funded by the Spanish Ministerio de Ciencia e Innovación MCIN/AEI/10.13039/501100011033, FEDER, UE. BER acknowledges support from the NIRCam

Science Team contract to the University of Arizona, NAS5-02115, and *JWST* Program 3215. BRP acknowledges support from grant PID2024-158856NA-I00 funded by the Spanish Ministerio de Ciencia e Innovación MCIN/AEI/10.13039/501100011033 and by 'ERDF A way of making Europe'. MSS acknowledges support by the Science and Technology Facilities Council (STFC) grant ST/V506709/1. HÜ acknowledges funding by the European Union (ERC APEX, 101164796). Views and opinions expressed are however those of the authors only and do not necessarily reflect those of the European Union or the European Research Council Executive Agency. Neither the European Union nor the granting authority can be held responsible for them. The research of CCW was supported by NOIRLab, which is managed by the Association of Universities for Research in Astronomy (AURA) under a cooperative agreement with the National Science Foundation. The authors acknowledge use of the Lux supercomputer at UC Santa Cruz, funded by NSF MRI grant AST 1828315. *JWST*/NIRCam contract to the University of Arizona NAS5-02115. JW gratefully acknowledges support from the Cosmic Dawn Center through the DAWN Fellowship. The Cosmic Dawn Center (DAWN) is funded by the Danish National Research Foundation under grant No. 140.

DATA AVAILABILITY

The data sets were derived from sources in the public domain: *JWST*/NIRSpec MSA and *JWST*/NIRCam data from MAST portal at https://mast.stsci.edu/portal/Mashup/Clients/Mast/Portal.html as well as our own reduction and analysis at https://jades.herts.ac.uk/DR4/ and https://jades.herts.ac.uk/search/

REFERENCES

Abazajian K. N. et al., 2009, ApJS, 182, 543
Alves de Oliveira C. et al., 2018, in Observatory Operations: Strategies, Processes, and Systems VII. p. 107040Q
Arrabal Haro P. et al., 2023, ApJ, 951, L22
Baker W. M., Maiolino R., Bluck A. F. L., Lin L., Ellison S. L., Belfiore F., Pan H.-A., Thorp M., 2022, MNRAS, 510, 3622
Baker W. M. et al., 2025a, MNRAS, 539, 557
Baker W. M. et al., 2025b, A&A, 697, A90
Barsanti S. et al., 2023, MNRAS, 526, 1613
Belli S. et al., 2024, Nature, 630, 54
Bezanson R. et al., 2024, ApJ, 974, 92
Bluck A. F. L., Maiolino R., Brownson S., Conselice C. J., Ellison S. L., Piotrowska J. M., Thorp M. D., 2022, A&A, 659, A160
Boyett K. et al., 2024, MNRAS, 535, 2
Bunker A. J. et al., 2023, A&A, 677, A88
Bunker A. J. et al., 2024, A&A, 690, A288
Cameron A. J., Katz H., Witten C., Saxena A., Laporte N., Bunker A. J., 2024, MNRAS, 534, 523
Cappellari M., 2023, MNRAS, 526, 3273
Carnall A. C. et al., 2023, Nature, 619, 716
Carniani S. et al., 2024, Nature, 633, 318
Castellano M. et al., 2024, ApJ, 972, 143
Choi J., Dotter A., Conroy C., Cantiello M., Paxton B., Johnson B. D., 2016, ApJ, 823, 102
Conroy C., Gunn J. E., White M., 2009, ApJ, 699, 486
Conroy C., Naidu R. P., Zaritsky D., Bonaca A., Cargile P., Johnson B. D., Caldwell N., 2019, ApJ, 887, 237
Curti M. et al., 2023, MNRAS, 518, 425
Curti M. et al., 2024, A&A, 684, A75
Curtis-Lake E. et al., 2023, Nat. Astron., 7, 622
Curtis-Lake E. et al., 2026, MNRAS
Dalton G. et al., 2012, in McLean I. S., Ramsay S. K., Takami H., eds, Proc. SPIE Conf. Ser. Vol. 8446, Ground-based and Airborne Instrumentation for Astronomy IV. SPIE, Bellingham, p. 84460P
Davies R. L. et al., 2024, MNRAS, 528, 4976
de Graaff A. et al., 2023, A&A, 684, A87
de Graaff A. et al., 2025a, Nat. Astron., 9, 280
de Graaff A. et al., 2025b, A&A, 697, A189
de Jong R. S. et al., 2019, The Messenger, 175, 3
DESI Collaboration, 2016, preprint (arXiv:1611.00036)
D'Eugenio F. et al., 2024a, Nat. Astron., 8, 1443
D'Eugenio F. et al., 2024b, A&A, 689, A152
D'Eugenio F. et al., 2025, ApJS, 277, 4
Dorner B., 2012, Theses, Université Claude Bernard – Lyon I, https://theses.hal.science/tel-00738070
Dorner B. et al., 2016, A&A, 592, A113
Driver S. P. et al., 2018, MNRAS, 475, 2891
Eisenstein D. J. et al., 2023a, ApJS, 283, 1
Eisenstein D. J. et al., 2023b, ApJS, 281, 2
Ferruit P. et al., 2022, A&A, 661, A81
Foreman-Mackey D., Hogg D. W., Lang D., Goodman J., 2013, PASP, 125, 306
Fruchter A. S., Hook R. N., 2002, PASP, 114, 144
Fujimoto S. et al., 2023, ApJ, 949, L25
Giardino G. et al., 2019, in Teuben P. J., Pound M. W., Thomas B. A., Warner E. M., eds, ASP Conf. Ser. Vol. 523, Astronomical Data Analysis Software and Systems XXVII. Astron. Soc. Pac., San Francisco, p. 645
Giavalisco M. et al., 2004, ApJ, 600, L93
Glazebrook K. et al., 2024, Nature, 628, 277
Goulding A. D. et al., 2023, ApJ, 955, L24
Graves G. J., Faber S. M., 2010, ApJ, 717, 803
Greene J. E. et al., 2024, ApJ, 964, 39
Hainline K. N. et al., 2024, ApJ, 976, 160
Harikane Y., Nakajima K., Ouchi M., Umeda H., Isobe Y., Ono Y., Xu Y., Zhang Y., 2024, ApJ, 960, 56
Horne K., 1986, PASP, 98, 609
Hsiao T. Y.-Y. et al., 2024, ApJ, 973, 81
Isobe Y. et al., 2025, MNRAS, 541, L71
Jakobsen P. et al., 2022, A&A, 661, A80
Ji X., Belokurov V., Maiolino R., Monty S., Isobe Y., Kravtsov A., McClymont W., Übler H., 2026, MNRAS, 545, 3
Johnson B. D. et al., 2026, preprint ()
Juodžbalis I. et al., 2024, MNRAS, 535, 853
Juodžbalis I. et al., 2025, MNRAS, 546, 3
Kauffmann G. et al., 2003a, MNRAS, 341, 33
Kauffmann G. et al., 2003b, MNRAS, 341, 54
Kocevski D. D. et al., 2023, ApJ, 954, L4
Kokorev V. et al., 2025, ApJ, 988, L10
Koller M., Maiolino R., Baker W. M., 2026, MNRAS, 545, 1
Kriek M. et al., 2015, ApJS, 218, 15
Looser T. J. et al., 2023, AAP, 697, A88
Looser T. J. et al., 2024, Nature, 629, 53
Lützgendorf N. et al., 2022, in Coyle L. E., Matsuura S., Perrin M. D., eds, Proc. SPIE Conf. Ser. Vol. 12180, Space Telescopes and Instrumentation 2022: Optical, Infrared, and Millimeter Wave. SPIE, Bellingham, p. 121800Y
Maiolino R. et al., 2020, The Messenger, 180, 24
Maiolino R. et al., 2024a, Nature, 627, 59
Maiolino R. et al., 2024b, A&A, 687, A67
Maiolino R. et al., 2026, MNRAS, 548, 1
Maseda M. V. et al., 2024, A&A, 689, A73
Naidu R. P. et al., 2025, The Open Journal of Astrophysics, 9, 56033
Nakajima K., Ouchi M., Isobe Y., Harikane Y., Zhang Y., Ono Y., Umeda H., Oguri M., 2023, ApJS, 269, 33
Nakajima K. et al., 2025, preprint (arXiv:2506.11846)
Oesch P. A. et al., 2023, MNRAS, 525, 2864
Oke J. B., Gunn J. E., 1983, ApJ, 266, 713

Peng Y.-j. et al., 2010, ApJ, 721, 193
Pérez-González P. G. et al., 2024, The Open Journal of Astrophysics, 9, 56033
Rauscher B. J. et al., 2012, in Holland A. D., Beletic J. W., eds, Proc. SPIE Conf. Ser. Vol. 8453, High Energy, Optical, and Infrared Detectors for Astronomy V. SPIE, Bellingham, p. 84531F
Rauscher B. J. et al., 2017, PASP, 129, 105003
Rawle T. D. et al., 2016, in MacEwen H. A., Fazio G. G., Lystrup M., Batalha N., Siegler N., Tong E. C., eds, Proc. SPIE Conf. Ser. Vol. 9904, Space Telescopes and Instrumentation 2016: Optical, Infrared, and Millimeter Wave. SPIE, Bellingham, p. 990446
Rawle T. D. et al., 2022, in Coyle L. E., Matsuura S., Perrin M. D., eds, Proc. SPIE Conf. Ser. Vol. 12180, Space Telescopes and Instrumentation 2022: Optical, Infrared, and Millimeter Wave. SPIE, Bellingham, p. 121803R
Rieke M. J. et al., 2023, ApJS, 269, 16
Robertson B. E. et al., 2026, preprint (arXiv:2601.15956)
Salpeter E. E., 1955, ApJ, 121, 161
Saxena A. et al., 2024, MNRAS, 548, stag808
Scholtz J. et al., 2025a, MNRAS, 545, staf2107
Scholtz J. et al., 2025b, A&A, 697, A175
Stott J. P. et al., 2016, MNRAS, 457, 1888
Strait V. et al., 2023, ApJ, 949, L23
Tamura N. et al., 2016, in Evans C. J., Simard L., Takami H., eds, Proc. SPIE Conf. Ser. Vol. 9908, Ground-based and Airborne Instrumentation for Astronomy VI. SPIE, Bellingham, p. 99081M
Treu T. et al., 2022, ApJ, 935, 110
Übler H. et al., 2023, A&A, 677, A145
Valentino F. et al., 2025, A&A, 699, A358
Vanzella E. et al., 2023, A&A, 678, A173
Vanzella E. et al., 2025, A&A, 705, L12
Walmsley M. et al., 2023, MNRAS, 526, 4768
Wang B. et al., 2023, ApJ, 957, L34
Weibel A. et al., 2025, ApJ, 983, 11
Wisnioski E. et al., 2015, ApJ, 799, 209
Witstok J. et al., 2025, Nature, 639, 897

APPENDIX A: EXTENSION OF FLAT-FIELD CURVE

As presented in Section 3, the pipeline requires three flat-field transmission curves, D-FLAT, S-FLAT, and F-FLAT, to process the MOS data and obtain the final flux-calibrated 1D and 2D spectra. The *JWST* CRDS provides the reference files for the flat-field for each disperser/filter configuration. However, all flat-field correction curves included in the reference files are defined only within the nominal wavelength ranges but the D-FLAT correction curve is already defined from 0.6 to 5.85 μm. Here, we discuss how we extended the curves of the F-FLAT and S-FLAT.

The F-FLAT curves depend mainly on the filters used in the selected disperse/filter configurations. R100 observations are obtained with the configuration PRISM/CLEAR that includes a bandpass filter, with both a cut-on and cut-off wavelength. The nominal maximal wavelength is 5.3 μm after which the transmission of the bandpass filter drops rapidly. However, we noted that a faint signal at a longer wavelength is recovered in both detectors. Therefore, we extended the wavelength range by performing a linear fitting of the curve between 5.2 and 5.3 μm and extending the profile up to 5.5 μm. The extended profile is shown in Fig. A1 as a dashed line. R1000 observations use long-pass filters, which have only a cut-on wavelength. The transmission throughputs of these filters are similar across overlapping wavelength ranges (see top panel of Fig. A1). Therefore, to extend the wavelength range of the reference files, we used the F-FLAT curves from the G140M/F100LP and G395M/F290LP configurations as proxies for the G140M/F070LP and G235M/F170LP configurations, respectively, beyond the nominal wavelength range. In the case of G395M/F290LP we performed a linear extrapolation of the curve up to 5.5 μm with the same method used for the PRISM/CLEAR. The final F-FLAT curves for the R1000 configurations are shown in Fig. A1.

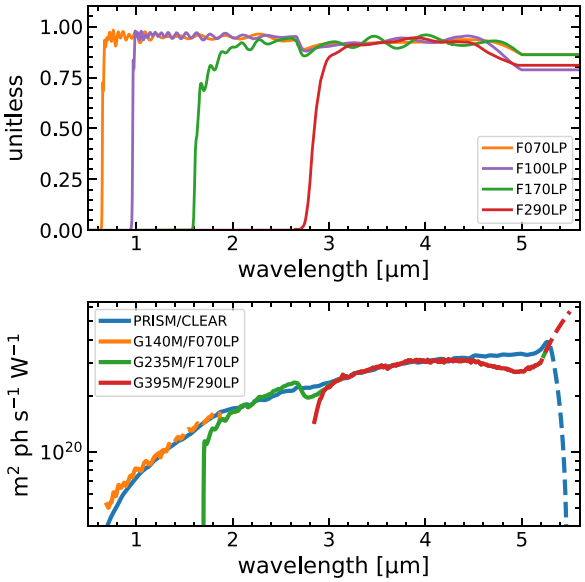

Figure A1. The top panel shows the transmission throughputs of the long-pass filters used in NIRSpec observations with the gratings. The bottom panel displays the F-FLAT curves applied to calibrate the data in this release. Dashed lines indicate the extrapolated portions of each curve, which extend the profiles beyond their nominal wavelength ranges.

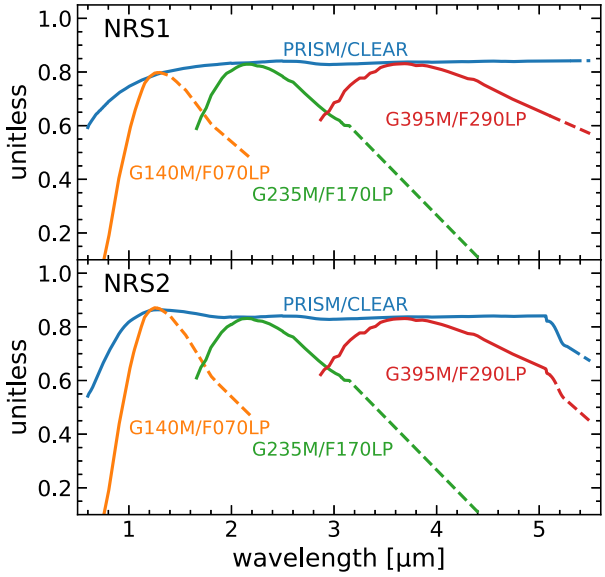

Figure A2. S-FLAT curves for each configuration and detector (NRS1 and NRS2) adopted to process the spectra of this data release. Dashed lines indicate the extrapolated portions of each curve, which extend the profiles beyond their nominal wavelength ranges.

The S-FLAT curves represent the photon conversion efficiency as a function of wavelength and depend primarily on the properties of the disperser. Since the G140M/F070LP

and G140M/F100LP configurations use the same grating, we used the S-FLAT curve from the latter to extend the reference file profile for the G140M/F070LP configuration. For the other three configurations-PRISM/CLEAR, G235M/F170LP, and G395M/F290LP-we fitted the S-FLAT curve over the final 0.1 μm of the nominal wavelength range using a first-order polynomial, and then used the best-fitting model to extrapolate the curve up to 5.5 μm. The final curves are shown in Fig. A2. We stress that the extrapolated curves are just a first-order approximation because we expect that the real curve include 'bump' and 'wiggles' in the profile, as we see in the nominal wavelength range of each configuration.

APPENDIX B: DATA-DRIVEN PATH-LOSS CORRECTION

The JADES NIRSpec pipeline, like the standard STScI pipeline, includes a step dubbed as 'pathloss', which calculates and applies corrections for each target in the MSA mask to account for signal losses along the optical path in the MOS spectroscopic mode. This correction is calculated assuming that all targets are point-like sources and using a PATHLOSS reference file that contains correction factors as functions of source position in the shutter aperture and wavelength. In the previous JADES data release (DR3; DE25), the pathloss correction was estimated using the PATHLOSS reference file *jwst_nirspec_pathloss_0005.fits* (first column in Fig. B1), which is based on detailed Fourier-optics simulations of the NIRSpec instrument carried out prior to the launch of *JWST* (P. Jakobsen et al. 2022).

For this data release, we opted to compute new pathloss corrections based on observations from *JWST* commissioning program 1133 (PI: Catarina Alves de Oliveira), which targeted 20 isolated stars in the Large Magellanic Cloud using the MOS mode. These stars were selected to be evenly distributed across the MSA field of view. Each star was observed 20 times, with its position varying within the shutter in each exposure. All stars have at least one exposure where the star is centred in the shutter, where the pathloss correction is expected to be negligible. This setup enables the construction of a shutter path-loss map by comparing the relative flux differences between spectra taken with the star at the shutter centre and those at different positions. Therefore, we processed the data with the standard pipeline but without applying any pathloss correction and comparing the final spectra. Here, we present how the data-based pathloss correction was derived from the individual 1D spectra of each star and exposure.

Fig. B2 illustrates the intra-shutter positions of all stars and exposures from the commissioning program 1133. The bi-dimensional histogram in the right panel shows the number of observations per 2D bin across the virtual shutter. The distribution reveals that the coverage of the shutter field of view is not uniform. The central region within 0.15 of the shutter pitch is well sampled, with more than 20 observations per bin, while the outer regions are more sparsely populated and, in some cases, entirely uncovered.

We created a reference file similar to that delivered by STScI which is a 3D datacube that samples the intrashutter position with a uniform 2D 31 × 31 grid, and a uniform wavelength array from 0.6 to 5.5 μm of 20 elements is used for the third axis of the cube. For each intra shutter position beam we estimated the path-loss correction as the median of the ratios between spectra at the centre of the shutter and the spectra obtained at the specific off-centre position. The results are shown in the second column

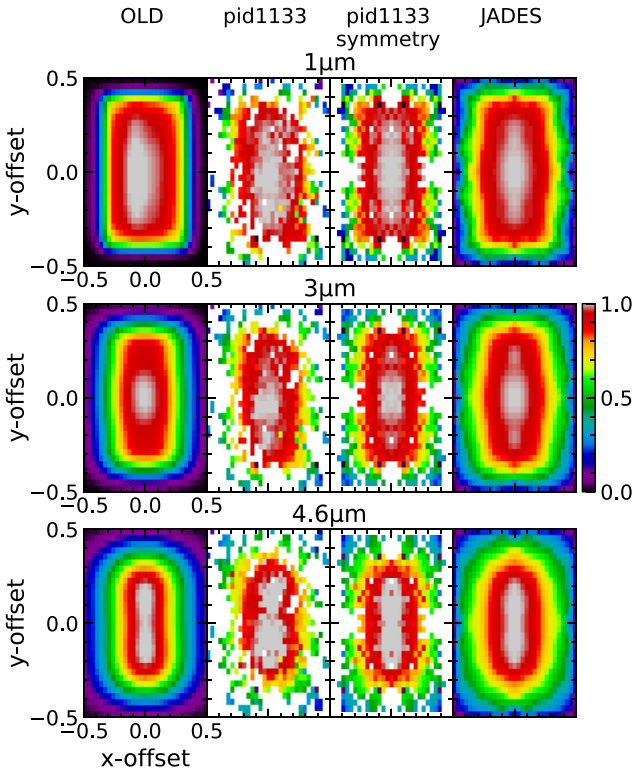

Figure B1. Path-loss correction maps for a point source at 1, 3, and 4.6 μm. The first column illustrates the correction maps adopted in DR3 and corresponding to the reference file *jwst_nirspec_pathloss_0005.fits*.The second column presents the estimates derived from the observations, while the third column reports the map obtained under the assumption of symmetry. The fourth column reports extrapolated path-loss corrections from the observations after performing a smoothing and linear interpolation in the region with no measurements. These are the correction maps adopted in this data release.

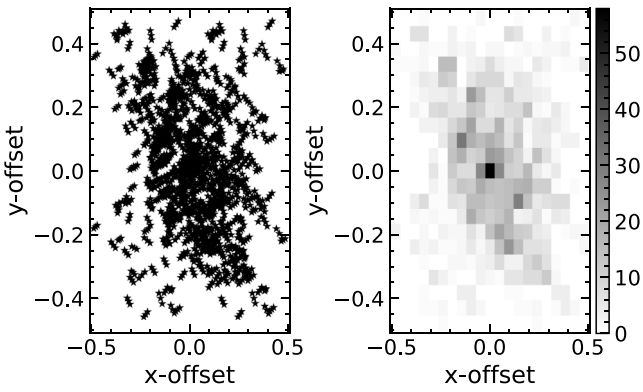

Figure B2. Placement of stars of program 1133 into operable MSA shutters. Left panels show each star's position in its own shutter, all plotted together in a single virtual shutter. The right panel presents a 2D histogram illustrating the distribution of stellar positions within this virtual shutter.

from the left of Fig. B1 at 1, 3 , and 4.6 μm. The empirical maps are somewhat different from the optical Fourier prediction (first column of the figure), but they have similar behaviour.

To improve the sampling, we assumed that the path-loss correction map is fully symmetric on both axes. This means that if

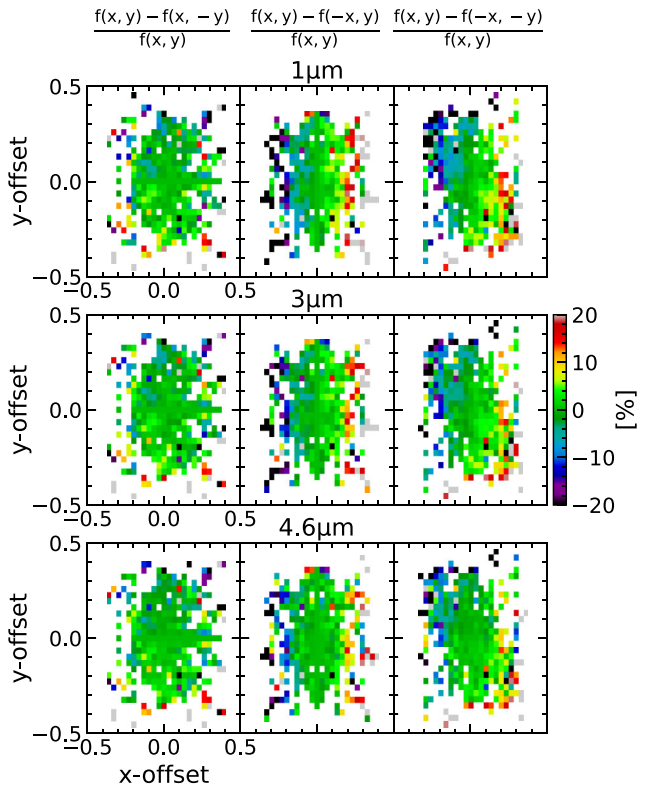

Figure B3. Path-loss correction maps for a point source at 1, 3, and 4.6 μm. The first column illustrates the correction maps adopted in DR3 and corresponding to the reference file *jwst_nirspec_pathloss_0005.fits*.The second column presents the estimates derived from the observations, while the third column reports the map obtained under the assumption of symmetry. The fourth column reports extrapolated path-loss corrections from the observations after performing a smoothing and linear interpolation in the region with no measurements. These are the correction maps adopted in this data release.

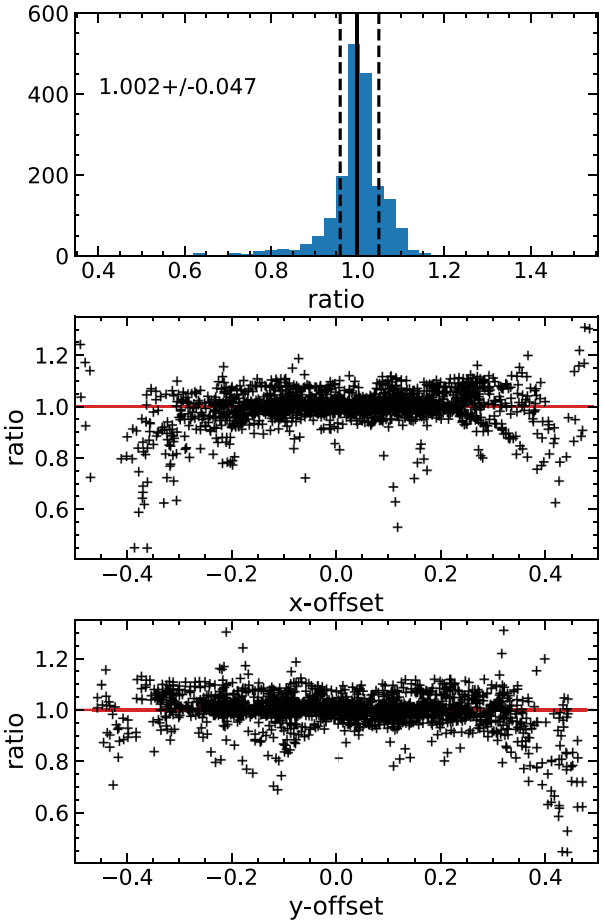

Figure B4. Ratios at 3 μm between spectra at the centre of the shutter and the spectra obtained at the specific off-centre position from the PID 1133 observation. The top panel shows the distribution of the ratio estimates. The text reports the corresponding median and standard deviation values. The middle and bottom panels illustrate the ratio estimates as a function of the intra-shutter position along the *x*- and *y*-directions, respectively.

the $f(x, y)$ is the correction at the intrashutter position (x, y), our assumption implies $f(-x, -y) = f(-x, y) = f(x, -y) = f(x, y)$. This allowed us to improve the sampling by a factor of four and decrease the uncertainties at the edges of the shutter.

We note, however, that this symmetry assumption may not be fully realistic. Fig. B1 illustrates the discrepancies in the path-loss maps, where measurements are available, that arise from enforcing symmetry. In particular, along the dispersion direction the path-loss map is not perfectly symmetric, and the error introduced by this assumption may be on the order of 10–20 per cent for targets located at $\sim 0.3-0.4$ of the shutter size from the centre. We emphasize that in these regions of the map only a limited number of measurements are available for each grid cell, and the uncertainties in the path-loss estimates may exceed those introduced by the symmetry assumption itself. Therefore, pending the acquisition of additional calibration observations, we adopt the symmetry assumption to construct the path-loss correction map.

Despite the assumption of symmetry along the *x*- and *y*-axes, the empirical maps still contained some bins with missing values. To address this, we performed a 2D linear interpolation to estimate the missing measurements, followed by a Gaussian smoothing with a standard deviation of 0.5 bins to suppress spurious fluctuations across the map. The final maps are shown in the third column of Fig. B1.

We validated the effectiveness of our data-based path-loss correction maps by reprocessing the data from commissioning program 1133 using the updated path-loss reference file. To assess the accuracy of the corrections, we estimated the flux ratios between spectra obtained at the centre of the shutter and those acquired at specific off-centre positions. Fig. B4 presents the distribution of ratio measurements at 3 μm. On average, the new path-loss corrections are quite accurate, with uncertainties below 5 per cent. However, when analysing the ratio estimates as a function of the intra-shutter position, we observe increased scatter towards the edges of the shutter (middle and bottom panels of Fig. B4). In particular, the corrections become less reliable when the target is located at a relative distance greater than 0.35 times the shutter pitch along either axis. This reduced accuracy is primarily due to the limited number of calibration observations at off-centre positions near the shutter edges.

We stressed that our path-loss reference files based on the PID 1133 are separate files compared to those released by the STScI in June 2025 (*jwst_nirspec_pathloss_0010.fits*). We compare our path-loss reference files with those from STScI in Fig. B5 . Our path losses have a different evolution with wavelength, better tracing the evolution of the NIRSpec PSF. Hence, sources well

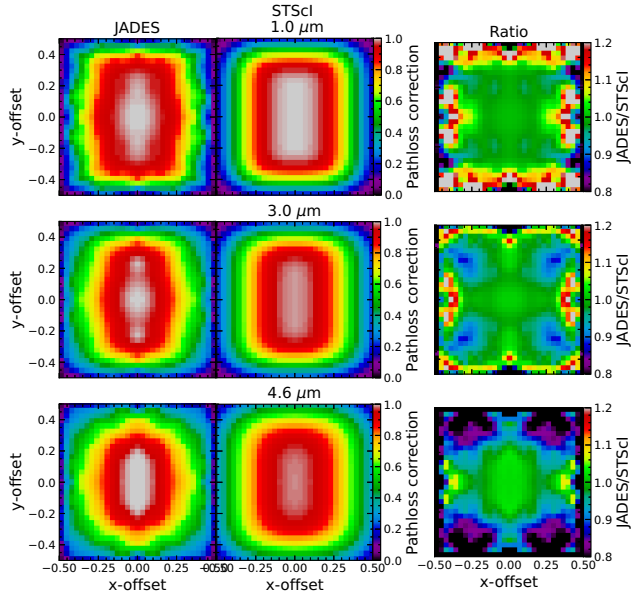

Figure B5. Comparison of our path-loss correction maps for a point source for our (JADES; first column) and STScI version *jwst_nirspec_pathloss_0010.fits* (second column) and the ratio between them (third column).

centred in the slit will not have any major differences between the different path-loss calibrations. However, sources towards the edges can differ by up to 30 per cent in their path-loss corrections and hence flux.

APPENDIX C: INTRA-SHUTTER POSITIONS OF TARGETS

The NIRSpec GTO pipeline relies on accurate knowledge of the intra-shutter positions of targets along the cross-dispersion direction, as provided by the MSA catalogue, in order to extract 1D spectra for each exposure. We therefore quantified the uncertainties associated with the target positions by comparing the values reported in the MSA catalogue with the photometric centroids estimated from the rectified PRISM/CLEAR 2D spectra. Specifically, for each exposure we constructed a surface-brightness profile and its associated uncertainties along the cross-dispersion direction by collapsing the 2D spectra along the spectral axis over the wavelength range between 2 and 4 μm. Profiles with peak SNRs below 10 were discarded, and a Gaussian function was fitted to the remaining profiles. The best-fitting centroids of the Gaussian profiles were adopted as the cross-dispersion positions of the sources. Fig. C1 shows the distribution of the discrepancy between the cross-dispersion positions derived from the MSA catalogue and the photometric centroids measured from the 2D spectra. We find no evidence for a systematic offset between the two sets of positions and conclude that the uncertainty in the target position along the cross-dispersion direction is approximately 0.04 arcsec, corresponding to less than half a detector pixel.

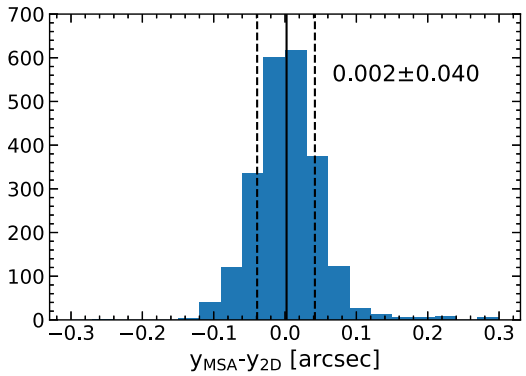

Figure C1. Distribution of the discrepancy between the cross-dispersion position derived from the MSA catalogue and the photometric centroid measured from the 2D spectra. The vertical lines indicate the 16th, 50th, and 84th percentiles of the distribution. The text reports the median and standard deviation.

APPENDIX D: WAVELENGTH OFFSET OF MAST FINAL PRODUCTS

In this appendix, we show the wavelength discrepancy between the prism and grating spectra delivered by the MAST archive. We calculate the wavelength offset by measuring the line centroid of the brightest rest frame optical line, such as [O III], Hα, and He I. The results are shown in Fig. D1 We find a systematic offset of about 0.5 nm between the line centroids measured with the prism and those obtained with the grating. This value

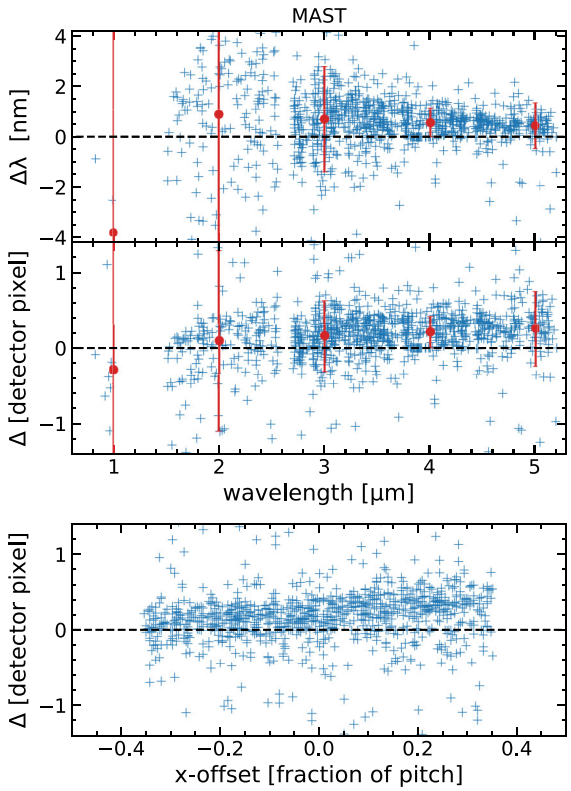

Figure D1. Top and middle panels show the wavelength offset in wavelength and detector pixel units between PRISM and R1000 MAST spectra as a function of wavelength. Red marks report the median and the standard deviation values of the distribution of measurements at 1, 2, 3, 4, and 5 μm. The bottom panel illustrates the wavelength offset in detector pixel units as a function of the intra-shutter location of the targets.

is consistent with the offset reported in DR3 (see Section 6.1). In addition, the spectral offset depends on the intra-shutter position of the targets, suggesting that the wavelength calibration step applied by the STScI pipeline does not provide an adequate correction.

[1]*Kavli Institute for Cosmology, University of Cambridge, Madingley Road, Cambridge CB3 0HA, UK*
[2]*Cavendish Laboratory, University of Cambridge, 19 JJ Thomson Avenue, Cambridge CB3 0HE, UK*
[3]*Scuola Normale Superiore, Piazza dei Cavalieri 7, I-56126 Pisa, Italy*
[4]*Centre for Astrophysics Research, Department of Physics, Astronomy and Mathematics, University of Hertfordshire, Hatfield AL10 9AB, UK*
[5]*Cosmic Dawn Center (DAWN), Rådmandsgade 64, 2200 København, Copenhagen, Denmark*
[6]*Niels Bohr Institute, University of Copenhagen, Jagtvej 128, DK-2200 Copenhagen, Denmark*
[7]*University of Oxford, Department of Physics, Denys Wilkinson Building, Keble Road, Oxford OX1 3RH, UK*
[8]*Centro de Astrobiología (CAB), CSIC-INTA, Cra. de Ajalvir Km. 4, E-28850 Torrejón de Ardoz, Madrid, Spain*
[9]*DARK, Niels Bohr Institute, University of Copenhagen, Jagtvej 155A, DK-2200 Copenhagen, Denmark*
[10]*Sorbonne Université, CNRS, UMR 7095, Institut d'Astrophysique de Paris, 98 bis bd Arago, F-75014 Paris, France*
[11]*Institut de Radioastronomie Millimétrique (IRAM), 300 Rue de la Piscine, F-38400 Saint-Martin-d'Hères, France*
[12]*European Southern Observatory, Karl-Schwarzschild-Strasse 2, D-85748 Garching, Germany*
[13]*Center for Astrophysics | Harvard & Smithsonian, 60 Garden St., Cambridge, MA 02138, USA*
[14]*Steward Observatory, University of Arizona, 933 N. Cherry Avenue, Tucson, AZ 85721, USA*
[15]*AURA for European Space Agency, Space Telescope Science Institute, 3700 San Martin Drive. Baltimore, MD 21210, USA*
[16]*Department of Physics and Astronomy, University College London, Gower Street, London WC1E 6BT, UK*
[17]*Department of Astronomy, University of Wisconsin-Madison, 475 N. Charter St., Madison, WI 53706, USA*
[18]*European Space Agency (ESA), European Space Astronomy Centre (ESAC), Camino Bajo del Castillo s/n, E-28692 Villafranca del Castillo, Madrid, Spain*
[19]*Space Telescope Science Institute, 3700 San Martin Drive, Baltimore, MD 21218, USA*
[20]*Department of Astronomy and Astrophysics, University of California, Santa Cruz, 1156 High Street, Santa Cruz, CA 95064, USA*
[21]*Max-Planck-Institut für extraterrestrische Physik (MPE), Gießenbachstraße 1, D-85748 Garching, Germany*
[22]*NSF National Optical-Infrared Astronomy Research Laboratory, 950 North Cherry Avenue, Tucson, AZ 85719, USA*
[23]*NRC Herzberg, 5071 West Saanich Rd, Victoria, BC V9E 2E7, Canada*

This paper has been typeset from a TEX/LATEX file prepared by the author.